
1 Local wind regime induced by giant linear dunes

2 Cyril Gadal · Pauline Delorme ·
3 Clément Narteau · Giles F.S. Wiggs ·
4 Matthew Baddock · Joanna M. Nield ·
5 Philippe Claudin

6
7 Received: DD Month YEAR / Accepted: DD Month YEAR

8 Abstract

9 Emergence and growth of sand dunes result from the interaction between the
10 topography, which perturbs the wind flow, which itself controls the sediment
11 transport. While these feedbacks are well studied at the scale of a single dune,
12 the average effect of a periodic dune pattern on atmospheric flows remains
13 poorly constrained due to a lack of data in major sand seas. Here, we compare
14 field measurements of surface wind data to the predictions of the ERA5-Land
15 climate reanalysis in four different places in Namibia, inside and north of the
16 giant-dune field of the Namib sand sea. In the flat desert areas to the north,
17 observations and predictions agree well despite the small amount of data in the
18 assimilation process. This is also the case in the interdune areas of the sand
19 sea, except for the weak winds blowing at night in a direction oblique to the

C. Gadal

Institut de Mécanique des Fluides de Toulouse, Université de Toulouse Paul Sabatier, CNRS,
Toulouse INP-ENSEEIHT, Toulouse, France. E-mail: cyril.gadal@imft.fr

P. Delorme

School of Geography and Environmental Science, University of Southampton, Southampton,
UK.

C. Narteau

Institut de Physique du Globe de Paris, Université de Paris, CNRS, Paris, France.

G.S.F. Wiggs

School of Geography and the Environment, University of Oxford, Oxford, UK.

M. Baddock

Geography and Environment, Loughborough University of Technology, Loughborough, UK.

J.M. Nield

School of Geography and Environmental Science, University of Southampton, Southampton,
UK.

P. Claudin

Physique et Mécanique des Milieux Hétérogènes, CNRS, ESPCI Paris, PSL Research
University, Université de Paris, Sorbonne Université, Paris, France. E-mail:
philippe.claudin@espci.fr

orientation of the giant dunes. We quantify these similarities and differences and provide a physical understanding of the relevant aerodynamical regimes to relate them to the daily cycle of the turbulent atmospheric boundary layer over a dune pattern of given wavelength. We conclude by identifying the conditions under which the ERA5-Land reanalysis data can or can't be used to study dune morphodynamics. We also propose that, in multidirectional wind regimes, deflections of specific winds could explain the occurrence of secondary dune patterns with a different orientation than the primary structures between which they grow.

Keywords Atmospheric boundary layer · Sand dunes · Fluid-structure interactions

31 1 Introduction

32 The description of turbulent flows over a complex topography is a rich and
33 active subject, that is relevant for a large variety of different environmental
34 systems (Finnigan et al. 2020). For example, the flow over hills is of primary
35 interest for wind power, meteorological and air pollution phenomena (Taylor
36 et al. 1987). The properties of these flows are also key to the understanding of
37 the formation of ocean surface wind-driven waves (Sullivan and McWilliams
38 2010), dissolution bedforms (Claudin et al. 2017), or sedimentary ripples and
39 dunes (Charru et al. 2013; Courrech du Pont 2015). Importantly, the tropo-
40 sphere presents a vertical structure, with a lower convective boundary layer,
41 of typical kilometer-scale thickness, capped by a stably stratified region (Stull
42 1988). The largest topographic obstacles as mountains can therefore interact
43 with this upper region, for example leading to internal wave generation or
44 significant wind disturbances, such as downslope winds in lee sides (Durran
45 1990).

46 Looking at the wind close to the surface, two topographic feedbacks on the
47 flow, although related, can be commented separately. There is a first effect on
48 the wind intensity: the flow accelerates on the upwind slope and slows down
49 on the downwind one (Baddock et al. 2011), with a speed-up factor essentially
50 proportional to the obstacle aspect ratio [here a ref?](#). Importantly, the velocity
51 maximum is typically shifted upwind of the obstacle crest. This behaviour has
52 been theoretically predicted by means of asymptotic analysis of a neutrally
53 stratified boundary-layer flow over an obstacle of vanishing aspect ratio (Jack-
54 son and Hunt 1975; Mason and Sykes 1979; Sykes 1980; Hunt et al. 1988;
55 Belcher and J.C.R. 1998). Experiments in flumes (Zilker et al. 1977; Zilker
56 and Hanratty 1979; Frederick and Hanratty 1988; Poggi et al. 2007), in wind
57 tunnel (Gong and Ibbetson 1989; Finnigan et al. 1990; Gong et al. 1996) and
58 in field conditions (Taylor and Teunissen 1987; Claudin et al. 2013; Fernando
59 et al. 2019; Lü et al. 2021), have also documented this effect. Interestingly, a
60 similar behaviour exists for the pressure perturbation, but with a slight down-
61 wind shift for the pressure minimum (Claudin et al. 2021). The second effect
62 is the flow deflection that occurs when the incident wind direction is not per-
63 pendicular to the ridge crest. While predicted to be small (less than 10°) in
64 the linear regime valid for shallow topography (Gadal et al. 2019), significant
65 flow steering has been reported in the field on the downwind side of steep
66 enough obstacles, such as mountain ranges (Kim et al. 2000; Lewis et al. 2008;
67 Fernando et al. 2019) or well developed sand dunes (Walker et al. 2009; Hesp
68 et al. 2015; Walker et al. 2017; Smith et al. 2017).

69 For practical reasons, wind measurement over sand dunes have been per-
70 formed over rather small bedforms, typically a few meters high only – that is
71 tens of meters in length. Giant dunes, with kilometer-scale wavelengths and
72 heights of tens of meters, are more difficult to investigate although they pro-
73 vide, for several reasons, a choice configuration for the study of turbulent flows
74 over a complex topography. First of all, one expects larger wind disturbances
75 for larger obstacles. Second, their large size make them interact with the verti-

76 cal structure of the atmosphere (Andreotti et al. 2009). Also, they usually form
77 large patterns in sand seas and thus behave as rather clean periodic pertur-
78 bations, in contrast with isolated hills. Finally, because the morphodynamics
79 of aeolian bedforms are strongly dependent on the local wind regime (Living-
80 stone and Warren 1996), one can expect to see the consequences of the wind
81 disturbances on smaller dunes, in a similar way as what has been reported for
82 the effect of dunes on impact ripples (Howard 1977; Hood et al. 2021).

83 Arid areas have been much studied at the desert scale from climate re-
84 analyses based on global atmospheric models (Blumberg and Greeley 1996;
85 Livingstone et al. 2010; Ashkenazy et al. 2012; Jolivet et al. 2021; Hu et al.
86 2021), such as ERA-40, ERA-Interim or ERA-5 (Uppala et al. 2005; Dee et al.
87 2011; Hersbach et al. 2020). However, the spatial resolution (tens of kilometers)
88 of these reanalyses implies average quantities that do not resolve the smaller
89 scales, ranging from individual dunes to the border of mountains (Livingstone
90 et al. 2010). Lately, the release of ERA5-Land allows to push back this limita-
91 tion by providing up to 70 years of hourly wind predictions at a 9 km spatial
92 resolution (Muñoz-Sabater et al. 2021). However, its validity remains to be
93 studied, especially in areas where data assimilation is low (such as deserts).

94 In this work, we compare local wind speeds and directions measured in four
95 different places inside and north of the giant-dune field of the Namib sand
96 sea to the regional predictions of the ERA5-Land climate reanalysis. When
97 the meteorological stations are surrounded by a relatively flat environment,
98 we show that local measurements and regional predictions agree well with
99 each other. We find that the agreement is also good in the interdune areas
100 of the sand sea, except for the weak winds blowing at night in a direction
101 oblique to the orientation of the giant dunes (section 2). Furthermore, we are
102 able to link the magnitude of these differences to the circadian cycle of the
103 atmospheric boundary layer (section 3). Finally, we draw implications of the
104 wind disturbances on smaller-scale dunes (section 4).

105 **2 Wind regimes across the Namib Sand Sea**

106 We have measured the wind regime in four different sites of Namibia, repre-
107 sentative of various environments across and nearby the Namib desert (Fig. 1).
108 The Adamax station is located near the Adamax salt pan, in a highly vege-
109 tated area. The Huab station, on the coast at the outlet of the Huab river, is in
110 an arid place where 60-m scale barchan dunes develop. These two stations are
111 located in a relatively flat [quantify how flat is flat ?](#) environment. In contrast,
112 the North Namib and South Namib stations are located in the interdune be-
113 tween tens of meters high giant linear dunes with kilometer-scale wavelengths
114 and superimposed patterns. In this section, we describe and compare winds
115 from local measurements and climate reanalysis predictions.

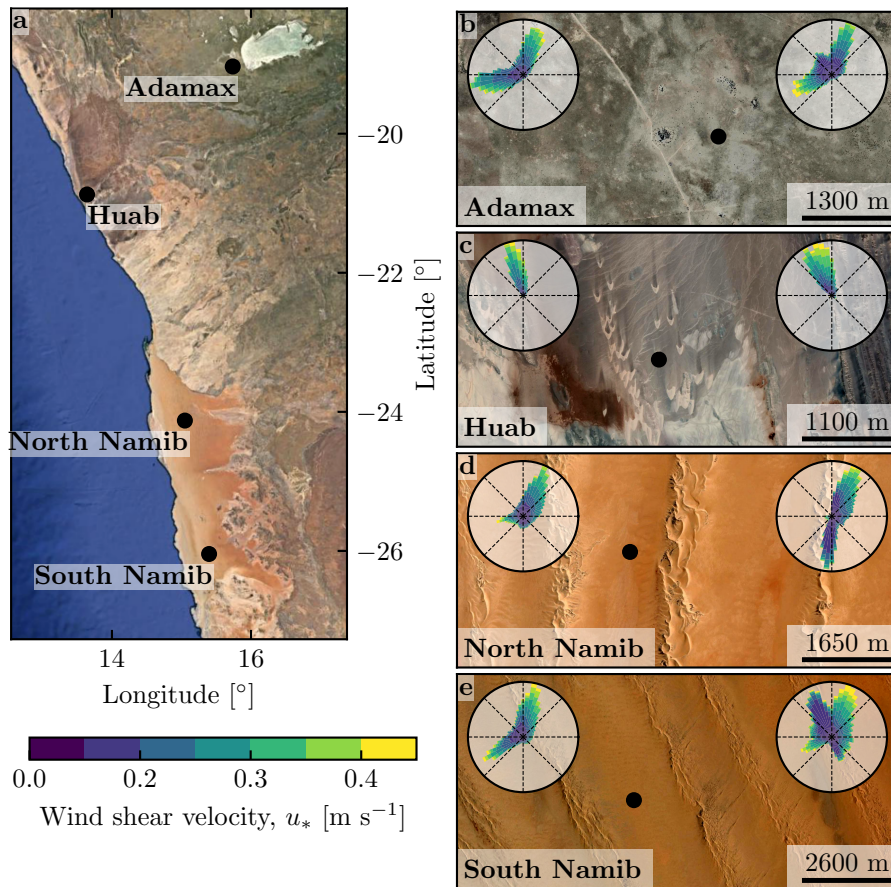


Fig. 1 Wind data used in this study **a:** Location of the different sites in Namibia. **b-e:** Satellite images of these different environments (Google-Earth, Maxar Technologies, CNES/Airbus). In each subplot, the left and right wind roses represent the data from the ERA5-Land climate reanalysis and the local wind stations, respectively. Note that the bars show the direction towards which the wind blows. The black dots show the location of local wind stations.

116 2.1 Wind and elevation data

117 Local winds are measured at meteorological stations located in these four
 118 different places (black dots in Fig. 1). The wind strength and direction are
 119 sampled every 10 minutes by cup anemometers and wind vanes, at heights
 120 between 2 m and 3 m depending on the station. The available period of mea-
 121 surements ranges from 1 to 5 discontinuous years distributed between 2012 and
 122 2020 (Suppl. Fig. S1). We checked that at least one complete seasonal cycle is
 123 available at each station. Regional winds are extracted at the same locations
 124 and periods from the ERA5-Land dataset, which is a replay at a smaller spatial
 125 resolution of ERA5, the latest climate reanalysis from the ECMWF (Hers-

¹²⁶ bach et al. 2020; Muñoz-Sabater et al. 2021). It provides hourly predictions
¹²⁷ of the 10-m wind velocity and direction at a spatial resolution of $0.1^\circ \times 0.1^\circ$
¹²⁸ (≈ 9 km in Namibia).

¹²⁹ For comparison, the local measurements are averaged into 1-hr bins cen-
¹³⁰ tered on the temporal scale of the ERA5-Land estimates (Suppl. Fig. S2). As
¹³¹ the wind velocities of both datasets are provided at different heights, we con-
¹³² vert them into shear velocities (Suppl. Mat. section 1), characteristic of the
¹³³ turbulent wind profile, which are then used together with the wind direction
¹³⁴ for further analysis. Wind roses in Fig. 1(b–e) show the resulting wind data.

¹³⁵ Dune properties are computed using autocorrelation on the 30-m Digital
¹³⁶ Elevation Models (DEMs) of the shuttle radar topography mission (Farr et al.
¹³⁷ 2007). For the South Namib and North Namib stations, we obtain respectively
¹³⁸ orientations of 85° and 125° with respect to the North, wavelengths of 2.6 km
¹³⁹ and 2.3 km and amplitudes of 45 m and 20 m (Suppl. Fig. S5 for more details).

¹⁴⁰ 2.2 Comparison of local and regional winds

¹⁴¹ The obtained wind regimes are shown in figure 1. In the Namib, the regional
¹⁴² wind patterns are essentially controlled by the see breeze, resulting in strong
¹⁴³ northward components (sometimes slightly deviated by the large scale topog-
¹⁴⁴ raphy mountain?) present in all regional wind roses (Lancaster 1985). These
¹⁴⁵ daytime winds are dominant during the second-half of the year (September-
¹⁴⁶ January). In winter, an additional easterly component can be recorded during
¹⁴⁷ the night, induced by the combination of katabatic winds forming in the moun-
¹⁴⁸ tains, and infrequent ‘berg’ winds, which are responsible of the high wind ve-
¹⁴⁹ locities observed (Lancaster et al. 1984). The frequency of these easterly com-
¹⁵⁰ ponents decreases from the inland to the coast. As a result, bidirectional wind
¹⁵¹ regimes within the Namib Sand Sea and at the Adamax salt pan (Fig. 1b,d,e)
¹⁵² and a unidirectional wind regime on the coast at the outlet of the Huab River
¹⁵³ (Fig. 1c) are observed.

¹⁵⁴ In the case of the Adamax and Huab stations, the time series of wind speed
¹⁵⁵ and direction from the regional predictions quantitatively match those corre-
¹⁵⁶ sponding to the local measurements (Fig. 2a–d) and Suppl. Fig. S5a–d, S6).
¹⁵⁷ For the North Namib and South Namib stations within the giant dune field,
¹⁵⁸ we observe that this agreement is also good, but limited to the September-
¹⁵⁹ January time period (Fig. 2e–h and Suppl. Fig. S5e–h). As a matter of
¹⁶⁰ fact, the measured wind roses exhibit additional wind components aligned with
¹⁶¹ the giant dune orientation, as evidenced on the satellite images (Fig. 1c,d).

¹⁶² More precisely, during the February-August period, the local and regional
¹⁶³ winds in the interdune match during daytime only, i.e when the southerly/southwesterly
¹⁶⁴ sea breeze dominates (Figs. 2e,f and 3, Suppl. Fig. S7). In the late afternoon
¹⁶⁵ and during the night, when the northwesterly ‘berg’ and katabatic winds blow,
¹⁶⁶ measurements and predictions differ. In this case, the angular wind distribu-
¹⁶⁷ tion of the local measurements exhibits two additional modes corresponding
¹⁶⁸ to reversing winds aligned with the giant dune orientation (purple frame in

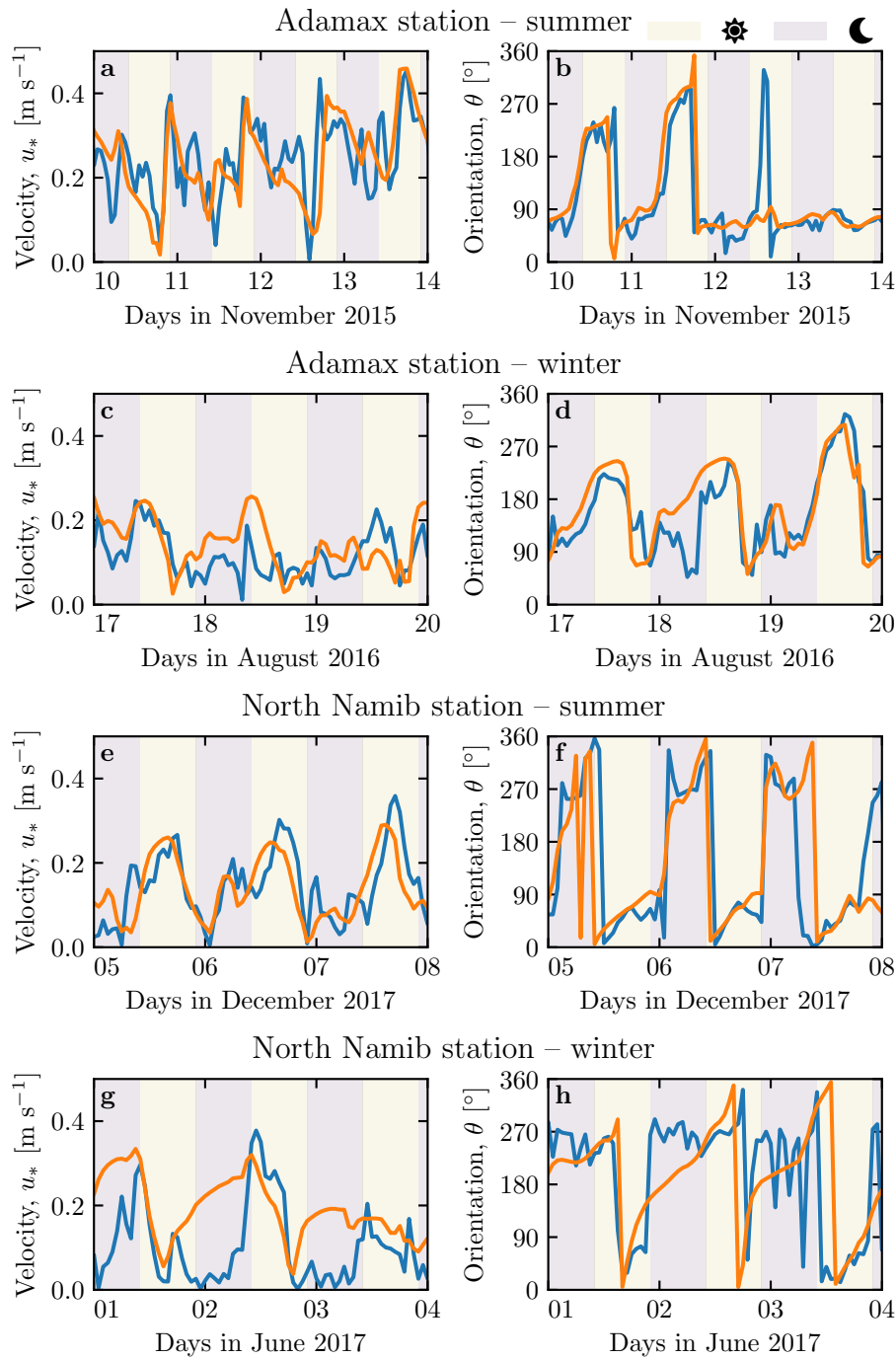


Fig. 2 Temporal comparison between the wind data coming from the ERA5-Land climate reanalysis (orange lines) and from the local measurements (blue lines). Coloured swathes indicate day (between 1000 UTC and 2200 UTC) and night (before 1000 UTC or after 2200 UTC). **a-b:** Adamax station in summer. **b-c:** Adamax station in winter. **d-e:** North Namib station in summer. **f-g:** North Namib station in winter. Time series of the two other stations are shown in Suppl. Fig. S4.

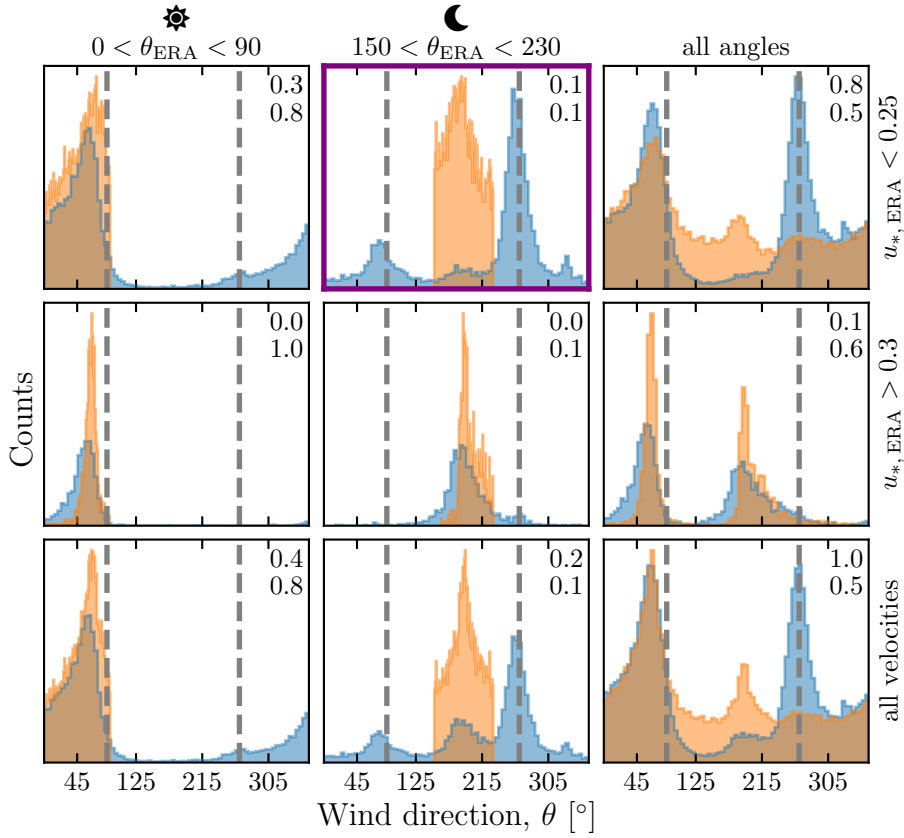


Fig. 3 Distributions of wind direction at the North Namib Station for the ERA5-Land climate reanalysis (orange) and the local measurements (blue). In each subplot, both distributions are plotted from the same time steps, selected with constraints on the wind direction (columns) and/or wind velocity (rows) of the ERA5-Land dataset. The gray vertical dashed lines indicate the dune orientation. The numbers at the top right give the percentage of time steps selected in each sub-range, as well as the percentage of them corresponding to the day (between 1000 UTC and 2200 UTC). The purple frame highlights the regime (small wind velocities, nocturnal summer wind) in which the data from both datasets differ. A similar figure can be obtained for the North Namib station (Suppl. Fig. S7).

169 Fig. 3, Suppl. Figs. S7 and S8). This deviation is also associated with a global
 170 attenuation of the wind strength (Suppl. Fig. S9). Remarkably, all these figures
 171 show that this wind reorientation and attenuation processes typically occur at
 172 low wind velocities, typically for $u_* \lesssim 0.1 \text{ m s}^{-1}$. For shear velocities larger
 173 than $\simeq 0.25 \text{ m s}^{-1}$, the wind reorientation is not significant. Finally, for inter-
 174 mediate shear velocities, moments of reorientation along the dune crest and
 175 others with no reorientation can both be observed (Suppl. Fig. S8). **CHECK**
 176 the above lines cf. δu

177 **3 Influence of wind speed and circadian cycle on the atmospheric
178 boundary layer**

179 The wind deflection induced by linear dunes has so far mainly been related
180 to the angle between wind direction and crest orientation, with a maximum
181 deflection for angles between 30° and 70° (Walker et al. 2009; Hesp et al. 2015).
182 In the analysed data, the most deflected wind at both North Namib and
183 South Namib stations is the most perpendicular to the giant dunes (Fig. ??).
184 The incident wind direction then does not seem to be the only parameter
185 controlling the wind deflection. In contrast, a different behaviour is observed
186 between low and high wind velocities, suggesting a change in hydrodynamical
187 regime. In this section, we discuss the relevant parameters associated with the
188 dynamical mechanisms that govern the interactions between the atmospheric
189 boundary layer flow and topographical obstacles. This analysis allows us to
190 provide a physics-based interpretation the observations.

191 **3.1 Flow over a modulated bed**

192 Taking as a reference the turbulent flow over a flat bed, the general framework
193 of this study is the understanding and the description of the flow response to
194 a bed modulation. Without loss of generality, we can consider in this con-
195 text an idealised bed elevation in the form of parallel sinusoidal ridges, with
196 wavelength λ (or wavenumber $k = 2\pi/\lambda$) and amplitude ξ_0 , and where the
197 reference flow direction makes a given angle with respect to the ridge crest
198 (Andreotti et al. 2012). Part of this response, on which we focus here, is the
199 flow deflection by the ridges. In a simplified way, it can be understood from
200 the Bernoulli principle (Hesp et al. 2015): as the flow approaches the ridge
201 crest, the compression of the streamlines results in larger flow velocities, and
202 thus lower pressures (Rubin and Hunter 1987). An incident flow oblique to
203 the ridge is then deflected towards lower pressure zones, i.e towards the crest.
204 Turbulent dissipation tends to increase this effect downstream, resulting in
205 along the crest wind deflection in the lee side (Gadal et al. 2019).

206 Flow confinement below a capping surface, which enhances streamline com-
207 pression, has a strong effect on the hydrodynamic response and typically in-
208 creases flow deflection. This is the case for bedforms forming in open channel
209 flows such as rivers (Fourrière et al. 2010; Unsworth et al. 2018). This is also
210 relevant for aeolian dunes as they evolve in the turbulent atmospheric bound-
211 ary layer (ABL) capped by the stratified free atmosphere (FA) (Andreotti et al.
212 2009). Two main mechanisms, associated with dimensionless numbers, must
213 then be considered (Fig. 4). First, topographic obstacles typically disturb the
214 flow over a characteristic height similar to their length. As flow confinement
215 is characterised by a thickness H , the interaction between the dunes and the
216 wind in the ABL is well captured by the parameter kH . The height H is di-
217 rectly related to the radiative fluxes at the Earth surface. It is typically on the
218 order of a kilometre, but significantly varies with the circadian and seasonal

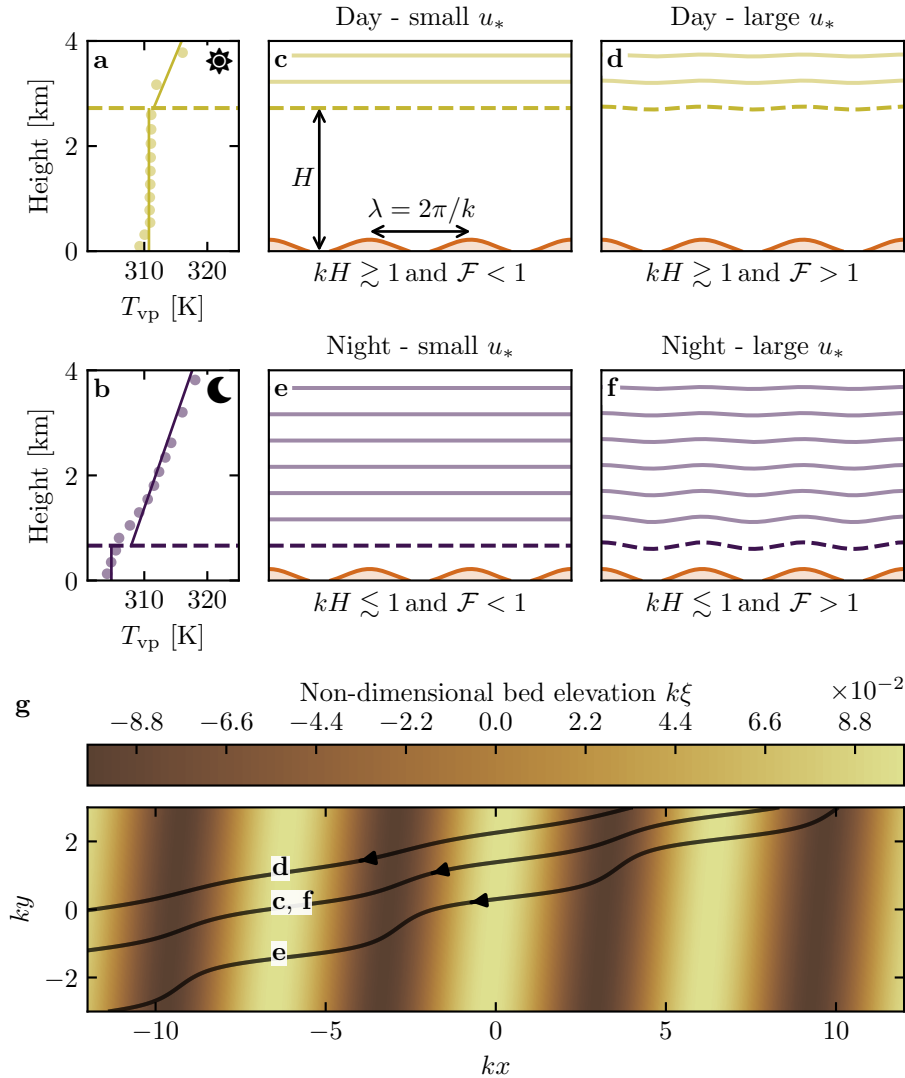


Fig. 4 **a-b:** Vertical profiles of the virtual potential temperature at 2 different time steps (day - 03/11/2015 - 1200 UTC, night - 01/13/2013 - 0900 UTC) at the North Namib station. Dots: data from the ERA5 reanalysis. Dashed lines: boundary layer height given by the ERA5 reanalysis (Suppl. Mat. section 2). Plain lines: vertical (boundary layer) and linear (free atmosphere) fits to estimate the stratification properties. **c-f:** Sketches representing the interaction between the giant dunes and the atmospheric flow for different meteorological conditions. **g:** Streamlines over a sinusoidal topography $\xi(x, y)$ qualitatively representing the effect of low, medium and strong flow confinement, in relation to the above panels (see Appendix 1 for more details). [add arrow with reference wind](#)

cycles. Emerging and small dunes, with wavelengths in the range 20 to 100 m, are not affected by the confinement, corresponding to $kH \gg 1$. For giant dunes with kilometric wavelengths, however, their interaction with the FA is significant (Andreotti et al. 2009). This translates into a parameter kH in the range 0.02–5, depending on the moment of the day and the season. A second important mechanism is associated with the existence of a thin intermediate so-called capping layer between the ABL and the FA. It is characterised by a density jump $\Delta\rho$, which controls the ‘rigidity’ of this interface, i.e. how much its deformation affects streamline compression. This is usually quantified using the Froude number (Vosper 2004; Stull 2006; Sheridan and Vosper 2006; Hunt et al. 2006; Jiang 2014):

$$\mathcal{F} = \frac{U}{\sqrt{\frac{\Delta\rho}{\rho_0} g H}}, \quad (1)$$

where U is the wind velocity at the top of the ABL and ρ_0 its average density. The intensity of the stratification, i.e. the amplitude of the gradient $|\partial_z \rho|$, also impact ability to deform the capping layer under the presence of an underlying obstacle, and thus affects the influence of flow confinement. This can be quantified using the internal Froude number (Vosper 2004; Stull 2006; Sheridan and Vosper 2006; Hunt et al. 2006; Jiang 2014) $\mathcal{F}_I = kU/N$, where $N = \sqrt{-g\partial_z \rho/\rho_0}$ is the Brunt-Väisälä frequency (Stull 1988). Both Froude numbers have in practice the same qualitative effect on flow confinement, and we shall restrict the main discussion to \mathcal{F} only.

This theoretical framework in mind, the smallest wind disturbances are expected to occur during the day, when the ABL depth is the largest and comparable to the dune wavelength ($kH \gtrsim 1$), which correspond to a weak confinement situation (Fig. 4c,d). On the contrary, large wind disturbances are expected to occur during the night, when the confinement is mainly induced by a shallow ABL (Fig. 4e). However, this strong confinement can be somewhat reduced in the case of strong winds, corresponding to large values of the Froude number (Fig. 4f). This is qualitative agreement with the transition from deflected to non-deflected winds related to low and high velocities observed in the data (Sec. 2.2).

3.2 Flow regime diagrams

We can go one step further and analyse how our data quantitatively spread over the different regimes discussed above. For that purpose, one needs to compute kH and \mathcal{F} from the time series. H , U and the other atmospheric parameters can be deduced from the various vertical profiles (temperature, humidity) available in the ERA5 climate reanalysis (Suppl. Mat. section 2). We quantify the flow deflection δ_θ as the minimal angle between the wind orientations comparing the local measurements and the regional predictions.

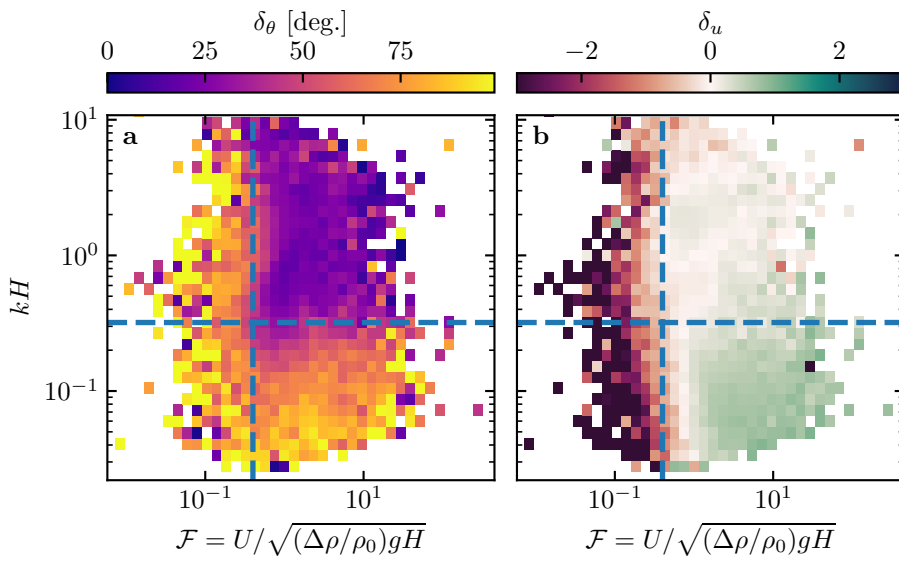


Fig. 5 Regime diagrams of the wind deviation δ_θ (a) and relative attenuation/amplification δ_u (b) in the space (\mathcal{F}, kH) , containing the data from both the North Namib and South Namib stations. Blue dashed lines empirically delimit the different regimes. The point density in each bin of the diagrams is shown in Suppl. Fig. S12. Similar regime diagrams in the spaces (\mathcal{F}_l, kH) and $(\mathcal{F}_l, \mathcal{F})$ are shown in Suppl. Fig. S13. ticks on x-axis ?

257 We also compute the relative velocity modulation as

$$\delta_u = \frac{u_*^{\text{ERA}} - u_*^{\text{station}}}{u_*^{\text{ERA}}}. \quad (2)$$

258 These two quantities are represented as maps in the plane (\mathcal{F}, kH) (Fig. 5a,b),
 259 and one can clearly identify different regions in these graphs. Small wind dis-
 260 turbances (small δ_θ and δ_u) are located in the top-right part of the diagrams,
 261 corresponding to a regime with low-interaction as well as low-confinement (kH
 262 and \mathcal{F} large enough, Fig. 4d). Lower values of kH (stronger interaction) or of
 263 Froude number (stronger confinement) both lead to an increase in wind dis-
 264 turbances, both in terms of orientation and velocity. Below a crossover value
 265 $kH \simeq 0.3$, wind disturbance is less sensitive to the \mathcal{F} -value, probably due to
 266 enhanced non-linear effects linked to strong flow modulation by the obstacle
 267 when confinement is strong more precise arguments?. The Froude number also
 268 controls a transition from damped to amplified wind velocities in the inter-
 269 dune, with a crossover around $\mathcal{F} \simeq 0.4$ (Fig. 5b). Such an amplification is
 270 rather unexpected. Checking the occurrence of the corresponding data, it ap-
 271 pears that they are mainly associated with the wind coming from the South,
 272 when it blows at the end of day, but in summer time only although it is also
 273 present in winter an additional suppl. fig. ?. This effect may be linked to a
 274 change in the flow behaviour in the lee side of the obstacle (lee waves, hy-

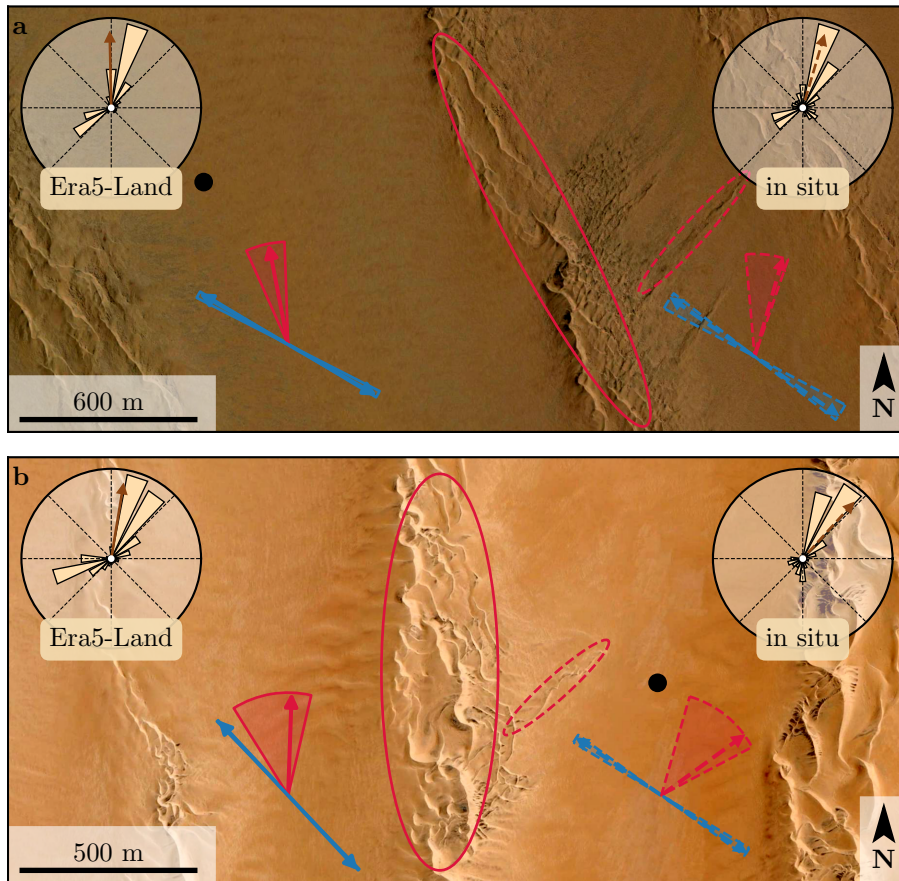


Fig. 6 Implications for smaller scale patterns in (a) the South Namib and (b) North Namib. The ellipses indicate the different types of elongating dunes, at large (plain line) and small (dashed line) scales. Dune orientation are predicted using the model of Courrech du Pont et al. (2014) from the sand flux angular distributions, shown here (roses and resultant transport direction) for typical values (grain size $180 \mu\text{m}$, flux-up ratio of 1.6). Code for corresponding arrows: use of ERA5-Land data (plain line), use of local measurements (dashed line), prediction for the bed instability growth mechanism (blue), prediction for the elongation growth mechanism (red). Wedges show the uncertainty on the orientation calculation when parameters are varied. The black dots indicate the location of the meteorological stations with respect to the dunes. See Appendix 2 for additional details.

275 hydraulic jumps, rotors) but further measurements are clearly needed in order
276 to assess the different possibilities (Baines 1995; Vosper 2004).

277 4 Discussion

278 The comparison of local (direct measurements) and regional (climate reanalysis)
279 wind data reveals the giant dune feedback on the wind flow. In flat areas,

the agreement between the two confirms the ability of the ERA5-Land climate reanalysis to predict the wind regime down to scales ~ 10 km, i.e the model grid. When smaller scale topographies are present (giant dunes in our case), locally measured winds can significantly differ from the regionally predicted ones. This is the case when the disturbances induced by the dunes interact with the lower part of the ABL vertical structure, which presents circadian variations. During the day, when the capping layer is typically high, this interaction is small, and the ERA5-Land predictions are also quantitatively consistent with the local data. During the night, however, the presence of a shallow atmospheric boundary layer induces a strong confinement of the flow, and is associated with large wind deflection by the dunes. Importantly, we find that this effect can be counterbalanced for large wind velocities, which are capable of deforming the capping layer, thus decreasing the influence of the confinement.

The theoretical computation of the wind disturbances induced by sinusoidal ridges under flow confinement has been performed in the linear limit (Andreotti et al. 2009, 2012), i.e. when the aspect ratio of these ridges is small ($k\xi_0 \ll 1$). These models are able to qualitatively reproduce the observed wind deflection (Appendix 1, Suppl. Figs. S13 and S14), and thus provide the physical support for the hydrodynamic picture we propose here. They however cannot reach the magnitude of these observations, probably due to the presence of expected non-linearities in high confinement situations linked to strong flow modulations. Besides, these linear calculations only predict wind attenuation in the interdune, in contrast with the observed enhanced velocities associated with particular summer evening winds from the South. Some other models also predict different spatial flow structures such as lee waves and rotors (Baines 1995; Vosper 2004), which of course cannot be observed by our single point measurements. Data at different places along and across the ridges are needed to investigate and possibly map such flow structures, and for further comparisons with the models.

This study highlights the interaction between giant dunes and the atmospheric boundary layer. It then supports the debated idea that the capping layer acts as a bounding surface impacting the dune dynamics, and limiting dune growth in particular (Andreotti et al. 2009), as opposed to an unconstrained growth ever-slower with size (Eastwood et al. 2011; Gunn et al. 2021). Interestingly, this mechanism would allow for the inference of the ABL depth from the giant bedforms spacing where measurements are not feasible or available, as e.g. performed by Lorenz et al. (2010) on Titan.

This interaction also has important implications for smaller scales bedforms, as illustrated in Fig. 6. In the Namib Sand Sea, small linear dunes (~ 50 m-wide) are present in the interdune between giant linear dunes (~ 2 km-wide). Strangely enough, the small dunes do not have the same orientation as the large ones, and sometimes denotes as ‘crossing dunes’. While differences between large and small scale dune patterns are observed ubiquitously, they are now largely attributed to the presence of two different dune growth mechanisms, leading to two different dune patterns (orientations and/or mor-

326 phologies) for the same wind regime (Courrech du Pont et al. 2014; Runyon
 327 et al. 2017; Lü et al. 2017; Song et al. 2019; Gadale et al. 2020; Hu et al. 2021).
 328 Here, however, we can get the orientations of the small and giant linear dunes
 329 from the same dune growth mechanism (elongating mode), respectively using
 330 the locally measured and regionally predicted winds (red arrows in Fig. 6).
 331 The feedback of the giant dunes on the wind described in this study then pro-
 332 vides an explanation for the existence of these small linear dunes elongating
 333 across the interdune, as yet unresolved. Further studies are of course needed
 334 to confirm this hypothesis. These crossing dunes could provide additional con-
 335 straints for the inference of local winds from bedforms, similarly to what is
 336 currently performed on Mars using ripple orientations (Liu and Zimbelman
 337 2015; Hood et al. 2021).

338 **Acknowledgements** We would like to acknowledge the contributors of the following open-
 339 source python libraries, Matplotlib (Hunter 2007), Numpy (Harris et al. 2020) and Scipy
 340 (Virtanen et al. 2020), which provide an incredibly efficient ecosystem allowing scientific
 341 research in Python.

342 ERA5 and ERA5-Land datasets are publicly available at the Copernicus Climate Change
 343 Service (C3S) Climate Data Store. The locally measured wind data can be found at [up-](#)
 344 [load on public data repository](#). The digital elevation models from the Shuttle Radar To-
 345 graphy Mission are publicly available from Nasa servers, and can be downloaded at
 346 <https://dwtkns.com/srtm30m/>. Fully documented codes used to analyse this study are
 347 available at <https://github.com/Cgadal/GiantDunes> (will be made public upon acceptance
 348 of this manuscript for publication).

349 [citing all grants ...] [TOAD](#)

350 Appendix 1: Linear theory of wind response to topographic pertur- 351 bation

352 Following the work of Fourrière et al. (2010), Andreotti et al. (2012) and
 353 Andreotti et al. (2009), we briefly expose in this appendix the framework of
 354 the linear response of a turbulent flow to a topographic perturbation of small
 355 aspect ratio. As a general bed elevation can be decomposed into Fourier modes,
 356 we focus here on a sinusoidal topography:

$$\xi = \xi_0 \cos [k (\cos(\alpha)x + \sin(\alpha)y)], \quad (3)$$

357 which is also a good approximation for the giant dunes observed in the North
 358 Namib and South Namib Station (Fig. 1 and Suppl. Fig. S4). x and y are
 359 the streamwise and spanwise coordinates, $k = 2\pi/\lambda$ the wavenumber of the
 360 sinusoidal perturbation, and α its crest orientation with respect to the y -
 361 direction. The two components of the basal shear stress $\tau = \rho_0 u_* \mathbf{u}_*$, constant
 362 in the flat bottom reference case, can then be generically written as:

$$\tau_x = \tau_0 \left(1 + k \xi_0 \sqrt{\mathcal{A}_x^2 + \mathcal{B}_x^2} \cos [k (\cos(\alpha)x + \sin(\alpha)y) + \phi_x] \right), \quad (4)$$

$$\tau_y = \tau_0 k \xi_0 \sqrt{\mathcal{A}_y^2 + \mathcal{B}_y^2} \cos [k (\cos(\alpha)x + \sin(\alpha)y) + \phi_y], \quad (5)$$

363 where τ_0 is the reference basal shear stress on a flat bed. We have defined
 364 the phase $\phi_{x,y} = \tan^{-1}(\mathcal{B}_{x,y}/\mathcal{A}_{x,y})$ from the in-phase and in-quadrature hy-
 365 drodynamical coefficients $\mathcal{A}_{x,y}$ and $\mathcal{B}_{x,y}$. They are functions of k and of the
 366 flow conditions, i.e the bottom roughness, the vertical flow structure and the
 367 incident flow direction, and the theoretical framework developed in the above
 368 cited papers proposes methods to compute them in the linear regime.

369 Following Andreotti et al. (2012), the effect of the incident wind direction
 370 can be approximated by the following expressions:

$$\mathcal{A}_x = \mathcal{A}_0 \cos^2 \alpha, \quad (6)$$

$$\mathcal{B}_x = \mathcal{B}_0 \cos^2 \alpha, \quad (7)$$

$$\mathcal{A}_y = \frac{1}{2} \mathcal{A}_0 \cos \alpha \sin \alpha, \quad (8)$$

$$\mathcal{B}_y = \frac{1}{2} \mathcal{B}_0 \cos \alpha \sin \alpha, \quad (9)$$

371 where \mathcal{A}_0 and \mathcal{B}_0 are now two coefficients independent of the dune orientation
 372 α , corresponding to the transverse case ($\alpha = 0$). For a fully turbulent bound-
 373 ary layer capped by a stratified atmosphere, these coefficients depend on kH ,
 374 kz_0 , \mathcal{F} and \mathcal{F}_I (Andreotti et al. 2009). In this study, we assume a constant hy-
 375 drodynamic roughness $z_0 \simeq 1$ mm (Suppl. Mat. section 1). For the considered
 376 giant dunes, this leads to $kz_0 \simeq 2 \cdot 10^{-6}$, as their wavelength is $\lambda \simeq 2.4$ km (or
 377 $k \simeq 2 \cdot 10^{-3} \text{ m}^{-1}$). Values of z_0 extracted from field data indeed typically fall
 378 between 0.1 mm and 10 mm (Sherman and Farrell 2008; Field and Pelletier
 379 2018). Importantly, \mathcal{A}_0 and \mathcal{B}_0 do not vary much in the corresponding range
 380 of kz_0 (Fourrière et al. 2010), and the results presented here are robust with
 381 respect to this choice.

382 With capping a layer height and Froude numbers computed from the
 383 ERA5-Land time series, the corresponding \mathcal{A}_0 and \mathcal{B}_0 can be deduced, allowing
 384 to produce maps as displayed in Suppl. Fig. S13. Interestingly, it shows similar
 385 regimes as in the diagrams of Fig. 5 and Fig. S12a,b, supporting the physics pic-
 386 ture. However, the matching remains qualitative only. As a matter of fact, the
 387 linearity assumption of the theoretical framework requires $(|\tau| - \tau_0)/\tau_0 \ll 1$,
 388 which translates into $k\xi \sqrt{\mathcal{A}_0^2 + \mathcal{B}_0^2} \ll 1$. In our case, the giant dune morphol-
 389 ogy gives $k\xi_0 \simeq 0.1$, which means that one quits the regime of validity of the
 390 linear theory when the coefficient modulus $\sqrt{\mathcal{A}_0^2 + \mathcal{B}_0^2}$ becomes larger than a
 391 few units. In accordance with the theoretical expectations, these coefficients
 392 present values on the order of unity ($\mathcal{A}_0 \simeq 3$ and $\mathcal{B}_0 \simeq 1$) in unconfined situa-
 393 tions (Claudin et al. 2013; Lü et al. 2021). In contrast and as illustrated in
 394 Suppl. Fig. S12a,b, larger values are predicted in case of strong confinement,
 395 which does not allow us to proceed to further quantitative comparison with
 396 the data.

397 Finally, the linear model is also able to reproduce the enhancement of the
 398 flow deflection over the sinusoidal ridges when $\sqrt{\mathcal{A}_0^2 + \mathcal{B}_0^2}$ is increased (Suppl.
 399 Fig. S13). Here, using $k\xi_0 \simeq 0.1$ to be representative of the amplitude of the
 400 giant dunes at the North Namib station, the coefficient modulus is bounded
 401 to 10.

402 **Appendix 2: Sediment transport and dune morphodynamics**

403 We summarise in this appendix the sediment transport and dune morphodynamics
 404 theoretical framework leading to the prediction of sand fluxes and dune
 405 orientations from wind data.

406 *Sediment transport* — The prediction of sand fluxes from wind data has been
 407 a long standing issue in aeolian geomorphological studies (Fryberger and Dean
 408 1979; Pearce and Walker 2005; Sherman and Li 2012; Shen et al. 2019). Based
 409 on laboratory studies in wind tunnels (Rasmussen et al. 1996; Iversen and
 410 Rasmussen 1999; Creyssels et al. 2009; Ho et al. 2011), as well as physical
 411 considerations (Ungar and Haff 1987; Andreotti 2004; Durán et al. 2011; Pähzt
 412 and Durán 2020), it has been shown that the steady saturated saltation flux
 413 over a flat sand bed depends linearly on the shear stress:

$$\frac{q_{\text{sat}}}{Q} = \Omega \sqrt{\Theta_{\text{th}}} (\Theta - \Theta_{\text{th}}), \quad (10)$$

414 where Ω is a proportionality constant, $Q = d\sqrt{(\rho_s - \rho_0)gd/\rho_0}$ is a character-
 415 istic flux, $\Theta = \rho_0 u_*^2 / (\rho_s - \rho_0)gd$ the Shields number, and Θ_{th} its threshold
 416 value below which saltation vanishes. $\rho_s = 2.6 \text{ g cm}^{-3}$ and $d = 180 \mu\text{m}$ are
 417 the grain density and diameter, and g is the gravitational acceleration. The
 418 shear velocity, and consequently the Shields number as well as the sediment
 419 flux, are time dependent.

420 Recently, Pähzt and Durán (2020) suggested an additional quadratic term
 421 in Shields to account for grain-grain interactions within the transport layer at
 422 strong wind velocities:

$$\frac{q_{\text{sat}, t}}{Q} = \frac{2\sqrt{\Theta_{\text{th}}}}{\kappa\mu} (\Theta - \Theta_{\text{th}}) \left(1 + \frac{C_M}{\mu} [\Theta - \Theta_{\text{th}}] \right), \quad (11)$$

423 where $\kappa = 0.4$ is the von Kármán constant, $C_M \simeq 1.7$ a constant and $\mu \simeq 0.6$ is
 424 a friction coefficient, taken to be the avalanche slope of the granular material.
 425 The fit of this law to the experimental data of Creyssels et al. (2009) and Ho
 426 et al. (2011) gives $\Theta_{\text{th}} = 0.0035$. The fit of Eq. 10 on these same data similarly
 427 gives $\Omega \simeq 8$ and $\Theta_{\text{th}} = 0.005$. The sand flux angular distributions and the
 428 dune orientations in Fig. 6 are calculated using this law (11). We have checked
 429 that using the ordinary linear relationship (10) instead does not change the
 430 predicted dune orientations by more than a few degrees.

431 *Dune orientations* — Dune orientations are predicted with the dimensional
 432 model of Courrech du Pont et al. (2014), from the sand flux time series com-
 433 puted with the above transport law. Two orientations are possible depending
 434 on the mechanism dominating the dune growth: elongation or bed instabil-
 435 ity. The orientation α corresponding the bed instability is then the one that
 436 maximises the following growth rate (Rubin and Hunter 1987):

$$\sigma \propto \frac{1}{H_d W_d T} \int_0^T q_{\text{crest}} |\sin(\theta - \alpha)| dt, \quad (12)$$

437 where θ is the wind orientation measured with respect to the same reference
 438 as α , and H_d and W_d are dimensional constants respectively representing the
 439 dune height and width. The integral runs over a time T , which must be repre-
 440 sentative of the characteristic period of the wind regime. The flux at the crest
 441 is expressed as:

$$q_{\text{crest}} = q_{\text{sat}} [1 + \gamma |\sin(\theta - \alpha)|], \quad (13)$$

442 where the flux-up ratio γ has been calibrated to 1.6 using field studies, under-
 443 water laboratory experiments and numerical simulations. Predictions of the
 444 linear analysis of Gadal et al. (2019) give similar results.

445 Similarly, the dune orientation corresponding to the elongation mechanism
 446 is the one that verifies:

$$\tan(\alpha) = \frac{\langle q_{\text{crest}}(\alpha) \mathbf{e}_\theta \rangle \cdot \mathbf{e}_{WE}}{\langle q_{\text{crest}}(\alpha) \mathbf{e}_\theta \rangle \cdot \mathbf{e}_{SN}}, \quad (14)$$

447 where $\langle \cdot \rangle$ denotes a vectorial time average. The unitary vectors \mathbf{e}_{WE} , \mathbf{e}_{SN} and
 448 \mathbf{e}_θ are in the West-East, South-North and wind directions, respectively.

449 The resulting computed dune orientations, blue and red arrows in Fig. 6,
 450 then depend on a certain number of parameters (grain properties, flux-up ratio,
 451 etc.), for which we take typical values for aeolian sandy deserts. Due to the lack
 452 of measurements in the studied places, some uncertainties can be expected. We
 453 therefore run a sensibility test by calculating the dune orientations for grain
 454 diameters ranging from 100 μm to 400 μm and for a speed-up ratio between
 455 0.1 and 10 (wedges in Fig. 6).

456 **References**

- 457 Andreotti B (2004) A two-species model of aeolian sand transport. *J Fluid
Mech* 510:47–70
- 458 Andreotti B, Fourrière A, Ould-Kaddour F, Murray B, Claudin P (2009) Gi-
459 ant aeolian dune size determined by the average depth of the atmospheric
460 boundary layer. *Nature* 457:1120–1123
- 461 Andreotti B, Claudin P, Devauchelle O, Durán O, Fourrière A (2012) Bedforms
462 in a turbulent stream: ripples, chevrons and antidunes. *J Fluid Mech* 690:94–
463 128
- 464 Ashkenazy Y, Yizhaq H, Tsoar H (2012) Sand dune mobility under climate
465 change in the kalahari and australian deserts. *Climatic Change* 112:901–923
- 466 Baddock M, Wiggs G, Livingstone I (2011) A field study of mean and turbulent
467 flow characteristics upwind, over and downwind of barchan dunes. *Earth
468 Surf Process Landforms* 36:1435–1448
- 469 Baines PG (1995) Topographic effects in stratified flows. Cambridge university
470 press
- 471 Belcher S, JCR H (1998) Turbulent flow over hills and waves. *Annu Rev Fluid
472 Mech* 30:507–538
- 473 Blumberg DG, Greeley R (1996) A comparison of general circulation model
474 predictions to sand drift and dune orientations. *J Clim* 9:3248–3259
- 475 Charru F, Andreotti B, Claudin P (2013) Sand ripples and dunes. *Annu Rev
476 Fluid Mech* 45:469–493
- 477 Claudin P, Wiggs G, Andreotti B (2013) Field evidence for the upwind velocity
478 shift at the crest of low dunes. *Boundary-layer Meteorol* 148:195–206
- 479 Claudin P, Durán O, Andreotti B (2017) Dissolution instability and roughen-
480 ing transition. *J Fluid Mech* 832:R2
- 481 Claudin P, Louge M, Andreotti B (2021) Basal pressure variations induced by
482 a turbulent flow over a wavy surface. *Front Phys* 9:682,564
- 483 Courrech du Pont S (2015) Dune morphodynamics. *C R Physique* 16:118–138
- 484 Courrech du Pont S, Narteau C, Gao X (2014) Two modes for dune orientation.
485 *Geology* 42:743–746
- 486 Creyssels M, Dupont P, El Mohtar AO, Valance A, Cantat I, Jenkins JT, Pasini
487 JM, Rasmussen KR (2009) Saltating particles in a turbulent boundary layer:
488 experiment and theory. *J Fluid Mech* 625:47–74
- 489 Dee DP, Uppala SM, Simmons AJ, Berrisford P, Poli P, Kobayashi S, Andrae
490 U, Balmaseda M, Balsamo G, Bauer dP, et al. (2011) The era-interim re-
491 analysis: Configuration and performance of the data assimilation system. *Q
492 J R Meteorol Soc* 137:553–597
- 493 Durán O, Claudin P, Andreotti B (2011) On aeolian transport: Grain-scale
494 interactions, dynamical mechanisms and scaling laws. *Aeolian Res* 3:243–
495 270
- 496 Durran DR (1990) Mountain waves and downslope winds. In: *Atmospheric
497 processes over complex terrain*, Springer, pp 59–81
- 498 Eastwood E, Nield J, Baas A, Kocurek G (2011) Modelling controls on aeolian
499 dune-field pattern evolution. *Sedimentology* 58:1391–1406
- 500

- 501 Farr TG, Rosen PA, Caro E, Crippen R, Duren R, Hensley S, Kobrick M,
502 Paller M, Rodriguez E, Roth L, et al. (2007) The shuttle radar topography
503 mission. *Rev Geophys* 45
- 504 Fernando H, Mann J, Palma J, Lundquist JK, Barthelmie RJ, Belo-Pereira M,
505 Brown W, Chow F, Gerz T, Hocut C, et al. (2019) The perdigão: Peering
506 into microscale details of mountain winds. *Bull Amer Meteor Soc* 100:799–
507 819
- 508 Field JP, Pelletier JD (2018) Controls on the aerodynamic roughness length
509 and the grain-size dependence of aeolian sediment transport. *Earth Surf
510 Process Landforms* 43:2616–2626
- 511 Finnigan J, Raupach M, Bradley E, Aldis G (1990) A wind tunnel study
512 of turbulent flow over a two-dimensional ridge. *Boundary-layer Meteorol*
513 50:277–317
- 514 Finnigan J, Ayotte K, Harman I, Katul G, Oldroyd H, Patton E, Poggi D,
515 Ross A, Taylor P (2020) Boundary-layer flow over complex topography.
516 *Boundary-layer Meteorol* 177:247–313
- 517 Fourrière A, Claudin P, Andreotti B (2010) Bedforms in a turbulent stream:
518 formation of ripples by primary linear instability and of dunes by nonlinear
519 pattern coarsening. *J Fluid Mech* 649:287–328
- 520 Frederick KA, Hanratty TJ (1988) Velocity measurements for a turbulent non-
521 separated flow over solid waves. *Exp Fluids* 6:477–486
- 522 Fryberger SG, Dean G (1979) Dune forms and wind regime. A study of global
523 sand seas 1052:137–169
- 524 Gadal C, Narteau C, Courrech Du Pont S, Rozier O, Claudin P (2019) Incip-
525 ient bedforms in a bidirectional wind regime. *J Fluid Mech* 862:490–516
- 526 Gadal C, Narteau C, Courrech du Pont S, Rozier O, Claudin P (2020) Peri-
527 odicity in fields of elongating dunes. *Geology* 48:343–347
- 528 Gong W, Ibbetson A (1989) A wind tunnel study of turbulent flow over model
529 hills. *Boundary-layer Meteorol* 49:113–148
- 530 Gong W, Taylor P, Dörnbrack A (1996) Turbulent boundary-layer flow over
531 fixed aerodynamically rough two-dimensional sinusoidal waves. *J Fluid Mech*
532 312:1–37
- 533 Gunn A, Wanker M, Lancaster N, Edmonds D, Ewing R, Jerolmack
534 D (2021) Circadian rhythm of dune-field activity. *Geophys Res Lett*
535 48:e2020GL090,924
- 536 Harris CR, Millman KJ, van der Walt SJ, Gommers R, Virtanen P, Cournapeau
537 D, Wieser E, Taylor J, Berg S, Smith NJ, et al. (2020) Array program-
538 ming with numpy. *Nature* 585:357–362
- 539 Hersbach H, Bell B, Berrisford P, Hirahara S, Horányi A, Muñoz-Sabater J,
540 Nicolas J, Peubey C, Radu R, Schepers D, et al. (2020) The era5 global
541 reanalysis. *Q J R Meteorol Soc* 146:1999–2049
- 542 Hesp PA, Smyth TAG, Nielsen P, Walker IJ, Bauer BO, Davidson-Arnott R
543 (2015) Flow deflection over a foredune. *Geomorphology* 230:64–74
- 544 Ho TD, Valance A, Dupont P, Ould El Moctar A, Tuan Duc H, Valance A,
545 Dupont P, Ould El Moctar A (2011) Scaling laws in aeolian sand transport.
546 *Phys Rev Lett* 106:4–7

- 547 Hood DR, Ewing RC, Roback KP, Runyon K, Avouac JP, McEnroe M (2021)
548 Inferring airflow across martian dunes from ripple patterns and dynamics.
549 *Front Earth Sci* 9:702,828
- 550 Howard AD (1977) Effect of slope on the threshold of motion and its applica-
551 tion to orientation of wind ripples. *Geol Soc Am Bull* 88:853–856
- 552 Hu Z, Gao X, Lei J, Zhou N (2021) Geomorphology of aeolian dunes in the
553 western sahara desert. *Geomorphology* 392:107,916
- 554 Hunt J, Leibovich S, Richards K (1988) Turbulent shear flows over low hills.
555 *Q J R Meteorol Soc* 114:1435–1470
- 556 Hunt JCR, Vilenski GG, Johnson ER (2006) Stratified separated flow around
557 a mountain with an inversion layer below the mountain top. *J Fluid Mech*
558 556:105–119
- 559 Hunter JD (2007) Matplotlib: A 2d graphics environment. *Computing in sci-
560 ence & engineering* 9:90–95
- 561 Iversen JD, Rasmussen KR (1999) The effect of wind speed and bed slope on
562 sand transport. *Sedimentology* 46:723–731
- 563 Jackson PS, Hunt JCR (1975) Turbulent wind flow over a low hill. *Q J R
564 Meteorol Soc* 101:929–955
- 565 Jiang Q (2014) Applicability of reduced-gravity shallow-water theory to atmo-
566 spheric flow over topography. *J Atmos Sci* 71:1460–1479
- 567 Jolivet M, Braucher R, Dovchintseren D, Hocquet S, Schmitt J, ASTER Team
568 (2021) Erosion around a large-scale topographic high in a semi-arid sedimen-
569 tary basin: Interactions between fluvial erosion, aeolian erosion and aeolian
570 transport. *Geomorphology* 386:107,747
- 571 Kim HG, Patel VC, Lee CM (2000) Numerical simulation of wind flow
572 over hilly terrain. *Journal of wind engineering and industrial aerodynamics*
573 87:45–60
- 574 Lancaster J, Lancaster N, Seely M (1984) Climate of the central namib desert.
575 Madoqua 1984:5–61
- 576 Lancaster N (1985) Winds and sand movements in the namib sand sea. *Earth
577 Surf Process Landforms* 10:607–619
- 578 Lewis HW, Mobbs SD, Lehning M (2008) Observations of cross-ridge flows
579 across steep terrain. *Q J R Meteorol Soc* 134:801–816
- 580 Liu ZYC, Zimbelman JR (2015) Recent near-surface wind directions inferred
581 from mapping sand ripples on martian dunes. *Icarus* 261:169–181
- 582 Livingstone I, Warren A (1996) Aeolian geomorphology: an introduction. Ad-
583 dison Wesley Longman Ltd
- 584 Livingstone I, Bristow C, Bryant RG, Bullard J, White K, Wiggs GFS, Baas
585 ACW, Bateman MD, Thomas DSG (2010) The namib sand sea digital
586 database of aeolian dunes and key forcing variables. *Aeolian Res* 2:93–104
- 587 Lorenz R, Claudin P, Andreotti B, Radabaugh J, Tokano T (2010) A 3 km
588 atmospheric boundary layer on titan indicated by dune spacing and huygens
589 data. *Icarus* 205:719–721
- 590 Lü P, Narteau C, Dong Z, Rozier O, Du Pont SC (2017) Unravelling raked
591 linear dunes to explain the coexistence of bedforms in complex dunefields.
592 *Nature comm* 8:1–9

- 593 Lü P, Narteau C, Dong Z, Claudin P, Rodriguez S, An Z, Fernandez-Cascales
594 L, Gadal C, Courrech du Pont S (2021) Direct validation of dune instability
595 theory. *Proc Natl Acad Sci USA* 118
- 596 Mason P, Sykes R (1979) Flow over an isolated hill of moderate slope. *Q J R
597 Meteorol Soc* 105:383–395
- 598 Muñoz-Sabater J, Dutra E, Agustí-Panareda A, Albergel C, Arduini G, Bal-
599 samo G, Boussetta S, Chounga M, Harrigan S, Hersbach H, et al. (2021)
600 Era5-land: A state-of-the-art global reanalysis dataset for land applications.
601 *Earth Syst Sci Data* 13:4349–4383
- 602 Pähzt T, Durán O (2020) Unification of aeolian and fluvial sediment transport
603 rate from granular physics. *Phys Rev Lett* 124:168,001
- 604 Pearce KI, Walker IJ (2005) Frequency and magnitude biases in the 'Fryberger'
605 model, with implications for characterizing geomorphically effective winds.
606 *Geomorphology* 68:39–55
- 607 Pelletier JD, Field JP (2016) Predicting the roughness length of turbulent flows
608 over landscapes with multi-scale microtopography. *Earth Surface Dynamics*
609 4:391–405
- 610 Poggi D, Katul G, Albertson J, Ridolfi L (2007) An experimental investigation
611 of turbulent flows over a hilly surface. *Phys Fluids* 19:036,601
- 612 Rasmussen KR, Iversen JD, Rautaheimo P (1996) Saltation and wind flow
613 interaction in a variable slope wind tunnel. *Geomorphology* 17:19–28
- 614 Rubin DM, Hunter RE (1987) Bedform alignment in directionally varying
615 flows. *Science* 237:276–278
- 616 Runyon K, Bridges N, Ayoub F, Newman C, Quade J (2017) An integrated
617 model for dune morphology and sand fluxes on mars. *Earth Planet Sci Lett*
618 457:204–212
- 619 Seidel DJ, Zhang Y, Beljaars A, Golaz JC, Jacobson AR, Medeiros B (2012)
620 Climatology of the planetary boundary layer over the continental united
621 states and europe. *J Geophys Research* 117:D17,106
- 622 Shao Y (2008) Physics and modelling of wind erosion, vol 37. Springer Science
623 & Business Media
- 624 Shen Y, Zhang C, Huang X, Wang X, Cen S (2019) The effect of wind speed
625 averaging time on sand transport estimates. *Catena* 175:286–293
- 626 Sheridan PF, Vosper SB (2006) A flow regime diagram for forecasting lee
627 waves, rotors and downslope winds. *Meteorological Applications* 13:179–195
- 628 Sherman DJ, Farrell EJ (2008) Aerodynamic roughness lengths over movable
629 beds: Comparison of wind tunnel and field data. *J Geophys Res* 113:1–10
- 630 Sherman DJ, Li B (2012) Predicting aeolian sand transport rates: A reevalu-
631 ation of models. *Aeolian Res* 3:371–378
- 632 Smith AB, Jackson DWT, Cooper JAG (2017) Three-dimensional airflow and
633 sediment transport patterns over barchan dunes. *Geomorphology* 278:28–42
- 634 Song Q, Gao X, Lei J, Li S (2019) Spatial distribution of sand dunes and their
635 relationship with fluvial systems on the southern margin of the taklimakan
636 desert, china. *Geomatics, Natural Hazards and Risk* 10:2408–2428
- 637 Spalding DB (1961) A single formula for the law of the wall. *J Applied Mech*
638 28:455–458

- 639 Stull R (2006) 9 - the atmospheric boundary layer. In: Wallace JM, Hobbs PV
640 (eds) *Atmospheric Science* (Second Edition), second edition edn, Academic
641 Press, San Diego, pp 375–417
- 642 Stull RB (1988) An introduction to boundary layer meteorology, vol 13.
643 Springer Science & Business Media
- 644 Sullivan PP, McWilliams JC (2010) Dynamics of winds and currents coupled
645 to surface waves. *Annu Rev Fluid Mech* 42:19–42
- 646 Sykes RI (1980) An asymptotic theory of incompressible turbulent boundary-
647 layer flow over a small hump. *J Fluid Mech* 101:647–670
- 648 Taylor P, Teunissen H (1987) The Askervein hill project: overview and back-
649 ground data. *Boundary-layer Meteorol* 39:15–39
- 650 Taylor P, Mason P, Bradley E (1987) Boundary-layer flow over low hills.
651 *Boundary-layer Meteorol* 39:107–132
- 652 Ungar JE, Haff PK (1987) Steady state saltation in air. *Sedimentology* 34:289–
653 299
- 654 Unsworth C, Parsons D, Hardy R, Reesink A, Best J, Ashworth P, Keevil G
655 (2018) The impact of nonequilibrium flow on the structure of turbulence
656 over river dunes. *Water Resour Res* 54:6566–6584
- 657 Uppala SM, Källberg P, Simmons AJ, Andrae U, Bechtold VDC, Fiorino M,
658 Gibson J, Haseler J, Hernandez A, Kelly G, et al. (2005) The era-40 re-
659 analysis. *Q J R Meteorol Soc* 131:2961–3012
- 660 Valance A, Rasmussen K, Ould El Moctar A, Dupont P (2015) The physics
661 of aeolian sand transport. *C R Physique* 16:1–13
- 662 Virtanen P, Gommers R, Oliphant TE, Haberland M, Reddy T, Cournapeau
663 D, Burovski E, Peterson P, Weckesser W, Bright J, et al. (2020) Scipy 1.0:
664 fundamental algorithms for scientific computing in python. *Nature methods*
665 17:261–272
- 666 Vogelezang D, Holtslag A (1996) Evaluation and model impacts of alternative
667 boundary-layer height formulations. *Boundary-layer Meteorol* 81:245–269
- 668 Vosper SB (2004) Inversion effects on mountain lee waves. *Q J R Meteorol Soc*
669 130:1723–1748
- 670 Walker I, Davidson-Arnott R, Bauer B, Hesp P, Delgado-Fernandez I, Oller-
671 head J, Smyth T (2017) Scale-dependent perspectives on the geomorphology
672 and evolution of beach-dune systems. *Earth-Science Rev* 171:220–253
- 673 Walker IJ, Hesp PA, Davidson-Arnott RG, Bauer BO, Namikas SL, Ollerhead
674 J (2009) Responses of three-dimensional flow to variations in the angle of
675 incident wind and profile form of dunes: Greenwich dunes, prince edward
676 island, canada. *Geomorphology* 105:127–138
- 677 Zhang C, Li Q, Zhou N, Zhang J, Kang L, Shen Y, Jia W (2016) Field obser-
678 vations of wind profiles and sand fluxes above the windward slope of a sand
679 dune before and after the establishment of semi-buried straw checkerboard
680 barriers. *Aeolian Research* 20:59–70
- 681 Zilker DP, Hanratty TJ (1979) Influence of the amplitude of a solid wavy wall
682 on a turbulent flow. part 2. separated flows. *J Fluid Mech* 90:257–271
- 683 Zilker DP, Cook GW, Hanratty TJ (1977) Influence of the amplitude of a solid
684 wavy wall on a turbulent flow. part 1. non-separated flows. *J Fluid Mech*

686 **Local wind regime induced by giant linear dunes**
 687 — Supplementary Material —

688 **C. Gadal* · P. Delorme · C. Narteau · G.F.S. Wiggs · M. Baddock ·**
 689 **J.M. Nield · P. Claudin**

690

691 * Institut de Mécanique des Fluides de Toulouse, Université de Toulouse Paul
 692 Sabatier, CNRS, Toulouse INP-ENSEEIHT, Toulouse, France.

693 cyril.gadal@imft.fr

694 **1. Shear velocity and calibration of the hydrodynamical roughness**

695 As the regionally predicted and locally measured velocities are available at
 696 different heights, we can not compare them directly. We then convert all ve-
 697 locities into shear velocities u_* , characteristic of the turbulent velocity profile
 698 (Spalding 1961; Stull 1988):

$$\frac{u(z)}{u_*} = \frac{1}{\kappa} \ln \left(\frac{z}{z_0} \right), \quad (15)$$

699 where z is the vertical coordinate, $\kappa = 0.4$ the von Kármán constant and
 700 z_0 the hydrodynamic roughness. Several field measurements of hydrodynamic
 701 roughnesses are available [Here cite a few old/general papers on roughness](#). In
 702 the absence of sediment transport, it scales with the geometric features of the
 703 bed (Pelletier and Field 2016) [too specific paper? other older papers?](#). When
 704 transport occurs, it rather typically scales with the thickness of the transport
 705 layer. For aeolian saltation, this is controlled by the altitude of Bagnold's
 706 focal point (Durán et al. 2011; Valance et al. 2015), which depends on the
 707 wind velocity and grain properties (Sherman and Farrell 2008; Zhang et al.
 708 2016; Field and Pelletier 2018). Whether associated with geometric features
 709 or with sediment transport, its typical order of magnitude is the millimetre
 710 scale.

711 We do not have precise velocity vertical profiles to be able to deduce an
 712 accurate value of z_0 in the various environments of the meteorological stations
 713 (vegetated, arid, sandy). Our approach is to rather select the hydrodynamic
 714 roughness which allows for the best possible matching between the regionally
 715 predicted and locally measured winds, i.e. minimising the relative difference δ
 716 between the wind vectors of both datasets:

$$\delta = \frac{\sqrt{\langle \| \mathbf{u}_{*,\text{era}} - \mathbf{u}_{*,\text{station}} \|^2 \rangle}}{\sqrt{\langle \| \mathbf{u}_{*,\text{era}} \|^2 \rangle \langle \| \mathbf{u}_{*,\text{station}} \|^2 \rangle}}, \quad (16)$$

717 where $\langle \cdot \rangle$ denotes time average. This parameter is computed for values of z_0
 718 in ERA5-Land analysis ranging from 10^{-5} m to 10^{-2} m for the four different
 719 stations. Note that for the North Namib and South Namib stations, where the
 720 giant dunes feedback presumably affect the wind, we take into account the
 721 non-deflected winds only in the calculation of δ (with a 15° tolerance).

As shown in Suppl. Fig. S3, the minimum values of δ in the space (z_0^{ERA5Land} , z_0^{local}) form a line. We thus set the roughness in the ERA5-Land analysis to the typical value $z_0 = 10^{-3}$ m, and deduce the corresponding ones for the local stations. It leads to 2.7, 0.8, 0.1 and 0.5 mm for the Adamax, North Namib, Huab and South Namib stations, respectively. Importantly, this approach somewhat impacts the calculation of the shear velocities, but not that of the wind directions. As such, most of our conclusions are independent of such a choice. However, it may affect the magnitude of the wind velocity attenuation/amplification in flow confinement situations.

2. Computation of the ABL characteristics

The estimation of the non-dimensional numbers associated with the ABL requires the computation of representative meteorological quantities. In arid areas, the vertical structure of the atmosphere can be approximated by a well mixed convective boundary layer of height H , topped by the stratified free atmosphere (Stull 1988; Shao 2008). In this context, one usually introduces the virtual potential temperature T_{vp} , which is a constant T_0 inside the boundary layer, and increases linearly in the FA (Suppl. Fig. S9a):

$$T_{\text{vp}}(z) = \begin{cases} T_0 & \text{for } z \leq H, \\ T_0 \left(1 + \frac{\Delta T_{\text{vp}}}{T_0} + \frac{N^2}{g}(z - H) \right) & \text{for } z \geq H, \end{cases} \quad (17)$$

where ΔT_{vp} is the temperature discontinuity at the capping layer and $N = \sqrt{g\partial_z T_{\text{vp}}/T_0}$ is the Brunt-Väisälä frequency, characteristic of the stratification. Note that, under the usual Boussinesq approximation, temperature and air density variations are simply related by $\delta T_{\text{vp}}/T_0 \simeq -\delta\rho/\rho_0$ (see Suppl. Mat. of Andreotti et al. (2009)), so that N can equivalently be defined from the density gradient as next to Eq. 1.

The ERA5 dataset provides vertical profiles of the geopotential ϕ , the actual temperature T and the specific humidity η at given pressure levels P . The vertical coordinate is then calculated as:

$$z = \frac{\phi R_t}{g R_t - \phi}, \quad (18)$$

where $R_t = 6371229$ m is the reference Earth radius and $g = 9.81$ m s⁻² is the gravitational acceleration. One also computes the virtual potential temperature as:

$$T_{\text{vp}} = T \left[1 + \left(\frac{M_d}{M_w} - 1 \right) \eta \right] \left(\frac{P_0}{P} \right)^{R/C_p}, \quad (19)$$

where $P_0 = 10^5$ Pa is the standard pressure, $R = 8.31$ J/K is the ideal gas constant, $C_p \simeq 29.1$ J/K is the air molar heat capacity, and $M_w = 0.018$ kg/Mol

753 and $M_d = 0.029 \text{ kg/Mol}$ are the molecular masses of water and dry air respectively.
 754 The specific humidity is related to the vapour pressure p_w as

$$\eta = \frac{\frac{M_w}{M_d} p_w}{p - \left(1 - \frac{M_w}{M_d}\right) p_w}. \quad (20)$$

755 The ERA5 dataset also provides an estimate of the ABL depth H , based
 756 on the behaviour of the Richardson vertical profile. This dimensionless num-
 757 ber is defined as the ratio of buoyancy and flow shear terms, and can be
 758 expressed as $\text{Ri} = N^2 / (\partial_z u)^2$. It vanishes in the lower well-mixed layer where
 759 T_{vp} is constant, and increases in the stratified FA. Following the method and
 760 calibration of Vogelegang and Holtslag (1996); Seidel et al. (2012), the value
 761 $\text{Ri}(z) \simeq 0.25$ has been shown to be a good empirical criterion to give $z \simeq H$
 762 within a precision varying from 50% for the shallower ABL (e.g. at night) to
 763 20% for situations of stronger convection.

764 Examples of vertical profiles of the virtual potential temperature deduced
 765 from ERA5 are shown in Suppl. Fig. S9a. For each of them, an average tem-
 766 perature is computed below the ABL depth ($z < H$), and a linear function is
 767 fitted above, allowing us to extract the temperature jump ΔT_{vp} . Importantly,
 768 some profiles display a vertical structure that cannot be approximated by the
 769 simple form (17) used here (Suppl. Fig. S9b). In practice, we removed from
 770 the analysis all of those leading to the unphysical case $\Delta T_{\text{vp}} < 0$. We have
 771 noticed that these ‘ill-processed’ profiles dominantly occur in winter and are
 772 evenly spread across the hours of the day. Importantly, they represent $\simeq 12\%$
 773 of the data only (Suppl. Fig. S9c,d), and we are thus confident that this data
 774 treatment does not affect our conclusions.

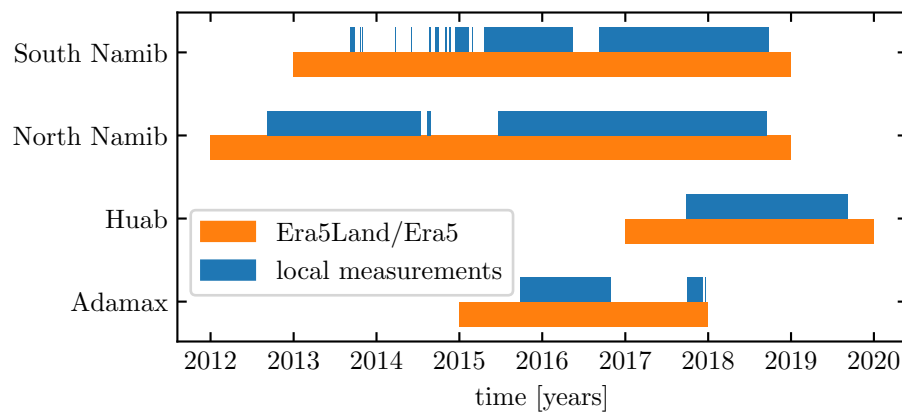


Fig. S1 Gant chart representing the valid time steps for the two data sets, for all stations.

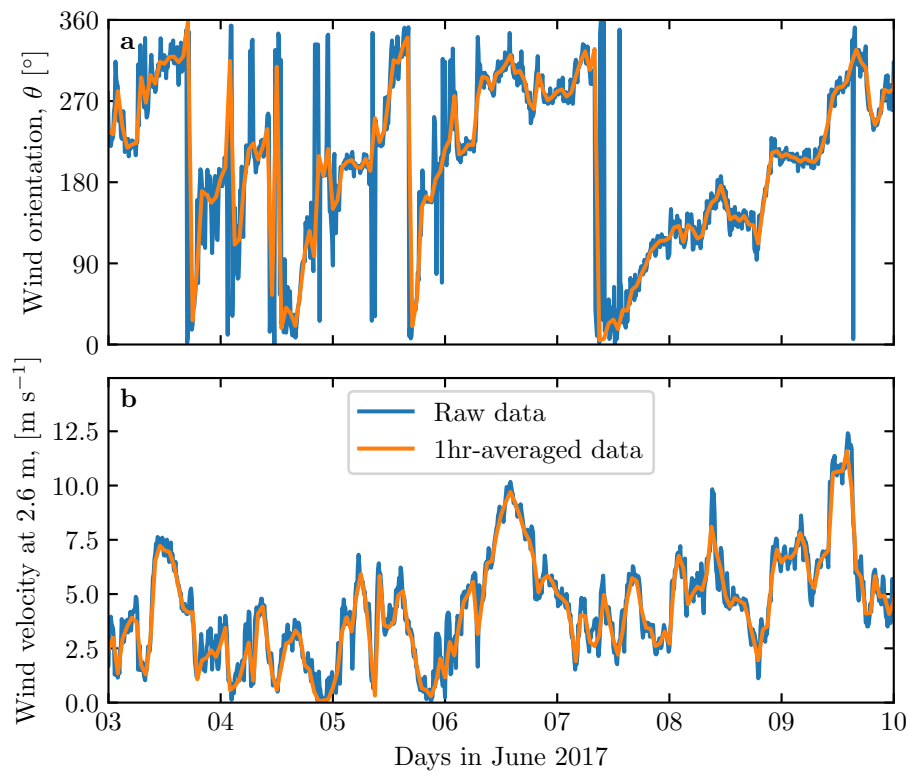


Fig. S2 Comparison between raw local wind measurements, and hourly-averaged data for South Namib station. **a:** wind direction. **b:** wind velocity at height 2.6 m.

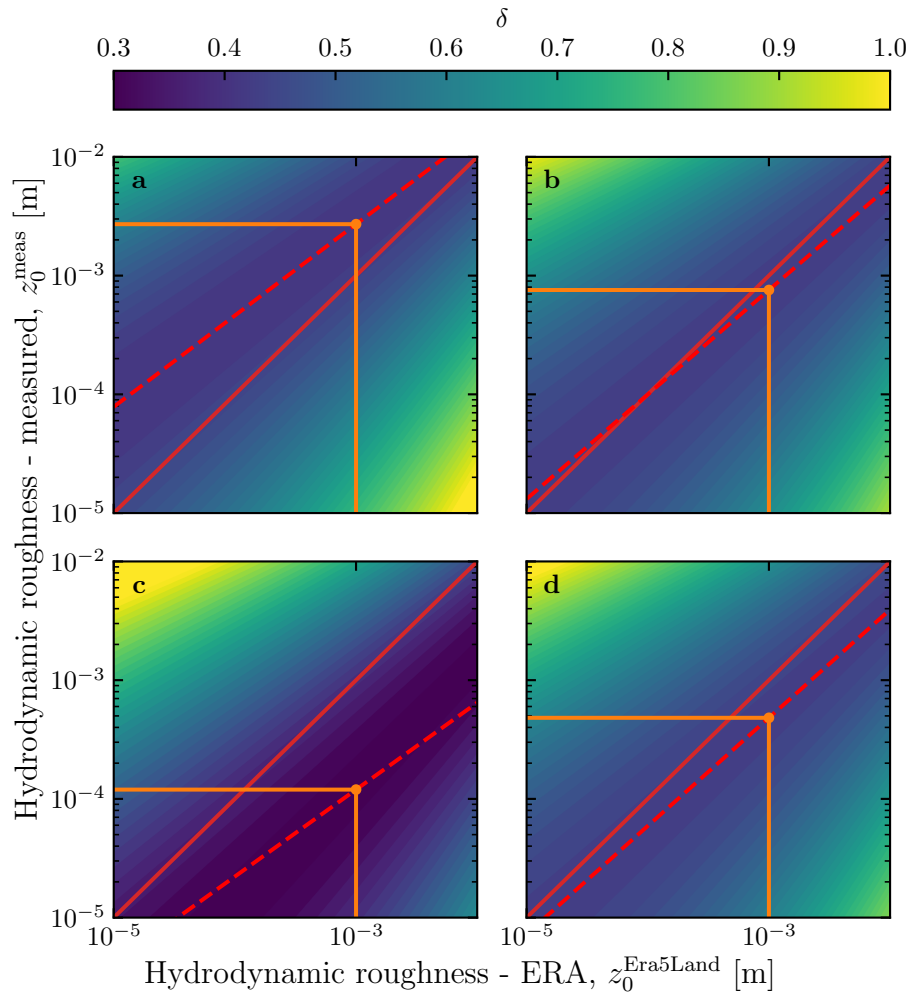


Fig. S3 Calibration of hydrodynamic roughness. The parameter δ (Eq. 16) quantifying the difference between local and predicted winds is shown in colorscale as a function of the hydrodynamic roughnesses chosen for the ERA5-Land and for local winds, for the (a) Adamax, (b) North Namib, (c) Huab and (d) South Namib stations. The red dashed and plain lines shows the minima of δ and the identity line, respectively. The orange lines and dots highlight the chosen hydrodynamic roughnesses for the local winds deduced from setting $z_0^{\text{ERA5Land}} = 1$ mm.

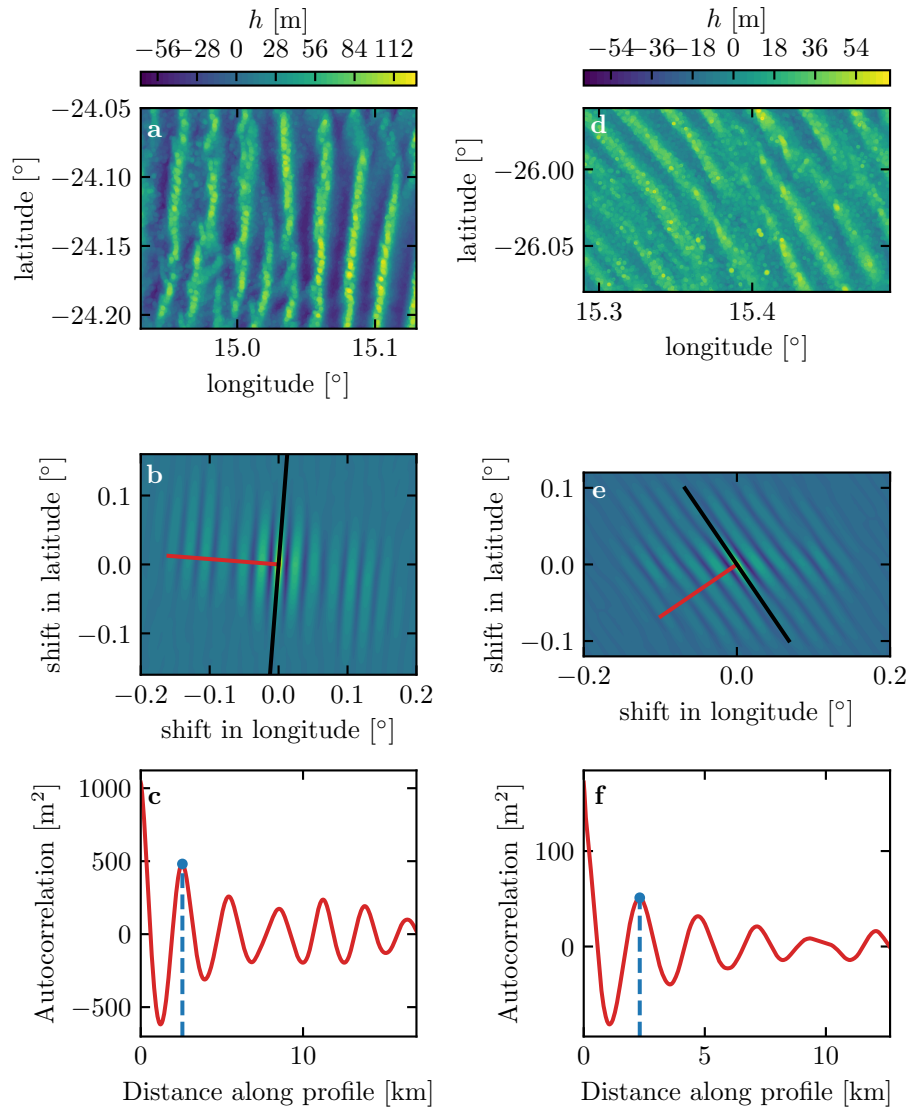


Fig. S4 Analysis of the DEMs of the North Namib (left column – panels **a**, **b**, **c**) and South Namib (right column – panels **d**, **e**, **f**) stations. **a-d**: Bed elevation detrended by a fitted second order polynomial base-line. **b-e**: Autocorrelation matrix shown in colorscale. The black line shows the detected dune orientation, and the red line represents the autocorrelation profile along which the dune wavelength is calculated, displayed in **c-f**. The blue lines and dots show the first peak of the autocorrelation profile, whose abscissa gives the characteristic wavelength of the dune pattern.

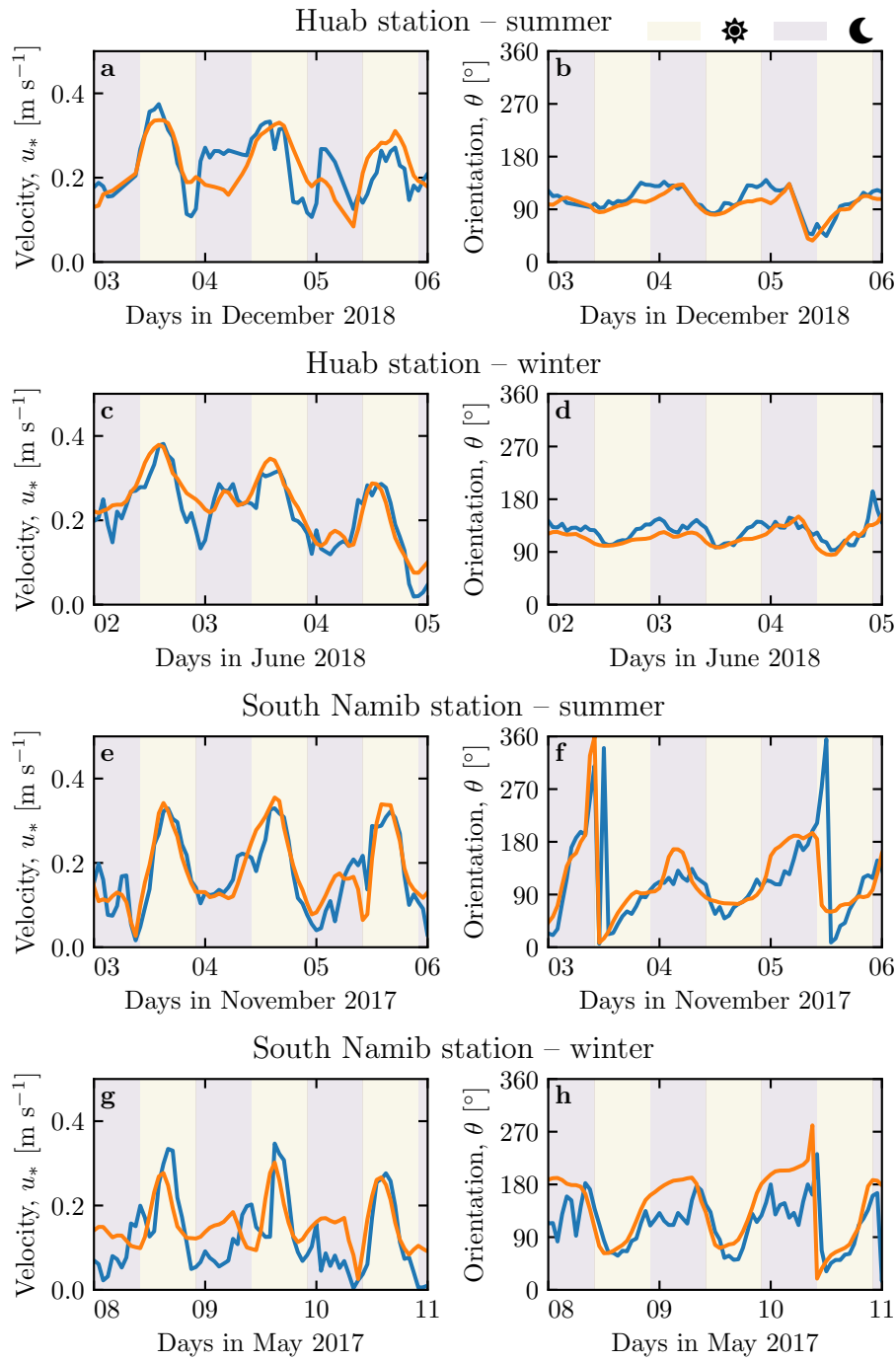


Fig. S5 Temporal comparison between the wind data coming from the ERA5-Land climate reanalysis (orange lines) and from the local measurements (blue lines). Coloured swathes indicate day (between 1000 UTC and 2200 UTC) and night (before 1000 UTC or after 2200 UTC). **a-b:** Huab station in summer. **b-c:** Huab station in winter. **d-e:** South Namib station in summer. **f-g:** South Namib station in winter.

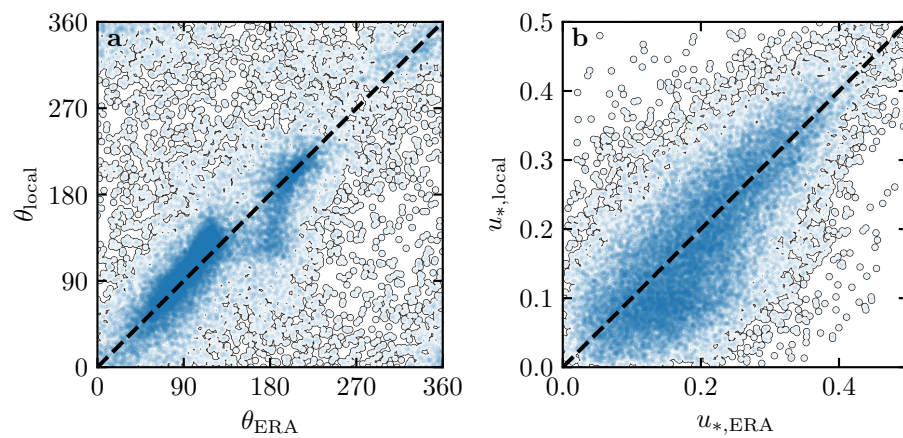


Fig. S6 Statistical comparison of the wind orientation (a) and velocity (b) between the ERA5-Land dataset and the local measurements for the Huab and Adamax stations. Data point clustering around identity lines (dashed and black) provide evidence for agreement of the two sets.

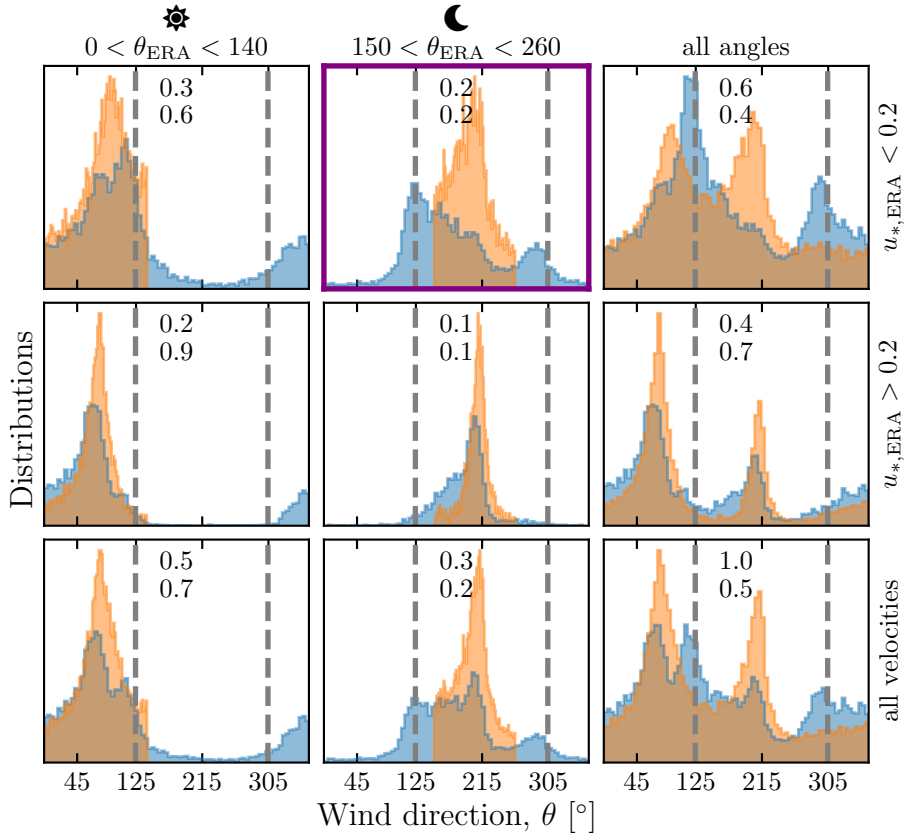


Fig. S7 Distributions of wind direction at the South Namib Station for the ERA5-Land climate reanalysis (orange) and the local measurements (blue) – equivalent of Fig. 3. In each subplot, both distributions are plotted from the same time steps, selected with constraints on the wind direction (columns) and/or wind velocity (rows) in the ERA5-Land dataset. The gray vertical dashed lines indicate the dune orientation. The numbers at the top centre give the percentage of time steps selected in each sub-range, as well as the percentage of them corresponding to the day (between 1000 UTC and 2200 UTC). The purple frame highlights the regime (small wind velocities, nocturnal summer wind) during which the wind data from both datasets differ.

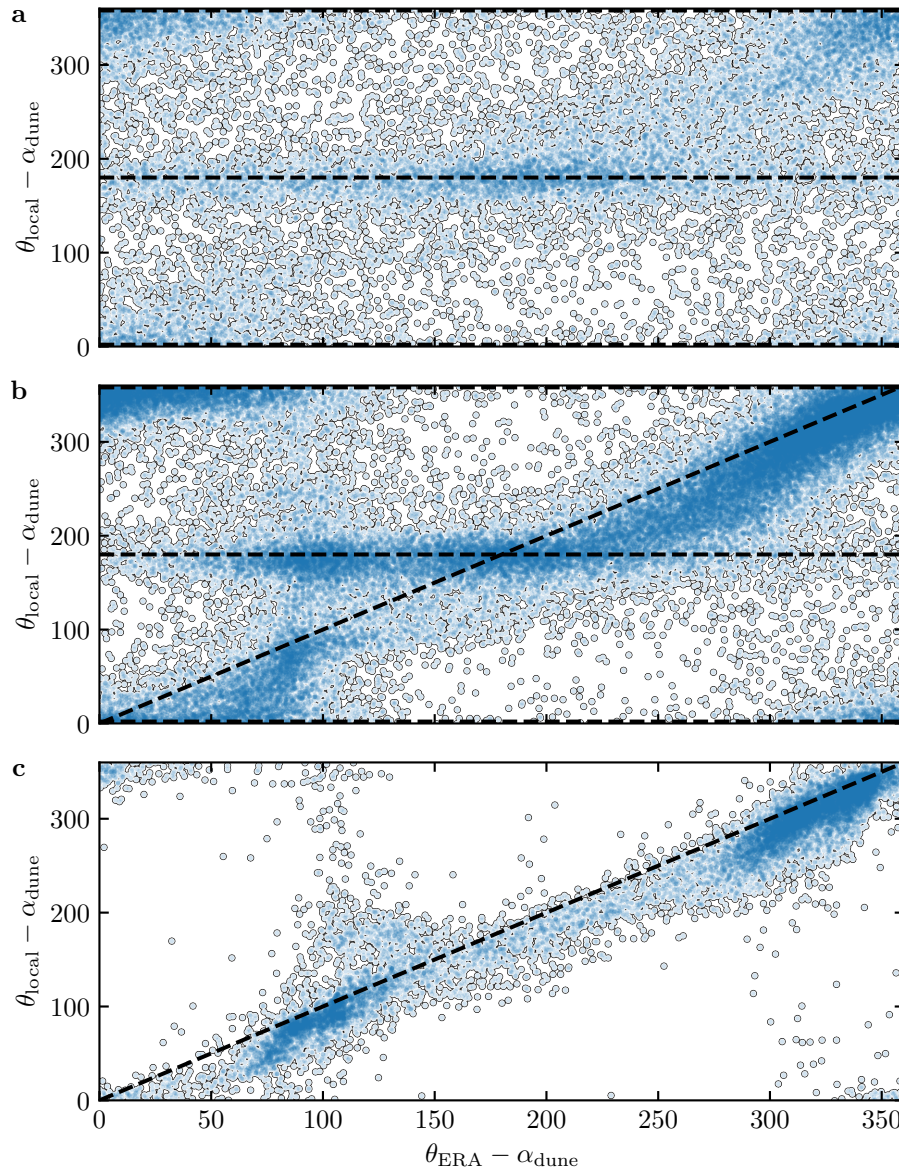


Fig. S8 Statistical comparison of the wind orientation between the ERA5-Land dataset and the local measurements for the South Namib and North Namib stations, for different velocity ranges. **a:** $u_{*,\text{ERA}} < 0.1 \text{ m s}^{-1}$. **b:** $0.1 < u_{*,\text{ERA}} \leq 0.25 \text{ m s}^{-1}$. **c:** $u_{*,\text{ERA}} \geq 0.25 \text{ m s}^{-1}$. The measured dune orientations are subtracted to the wind orientation, which allows us to plot both stations on the same graph. Black dashed lines indicate locally measured orientations aligned with the dune crests (here 0° , 180° and 360° – panels **a**, **b**), as well as the identity lines (panels **b**, **c**).

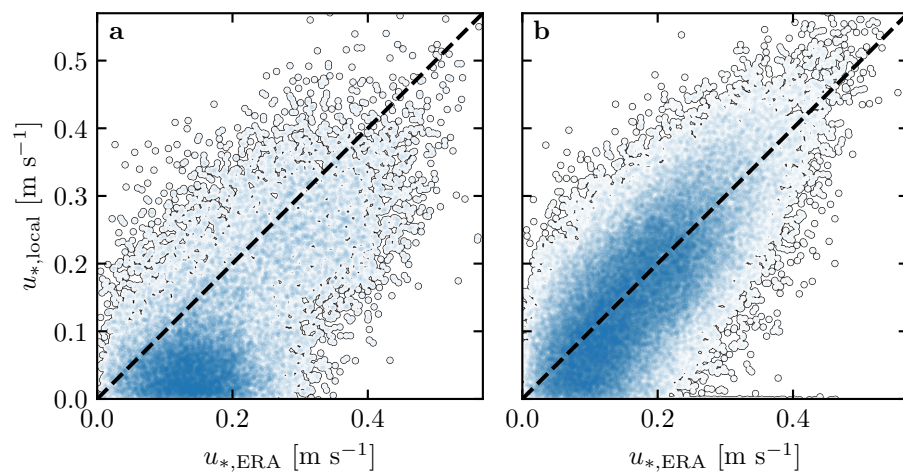


Fig. S9 Statistical comparison of the wind velocity between the ERA5-Land dataset and the local measurements for the South Namib and North Namib stations. **a:** Nocturnal summer easterly wind. **b:** Diurnal southerly wind. Black dashed lines are identity lines. The angle ranges used to select diurnal and nocturnal summer winds are the same as those in Fig. 3 and Suppl. Fig. S6.

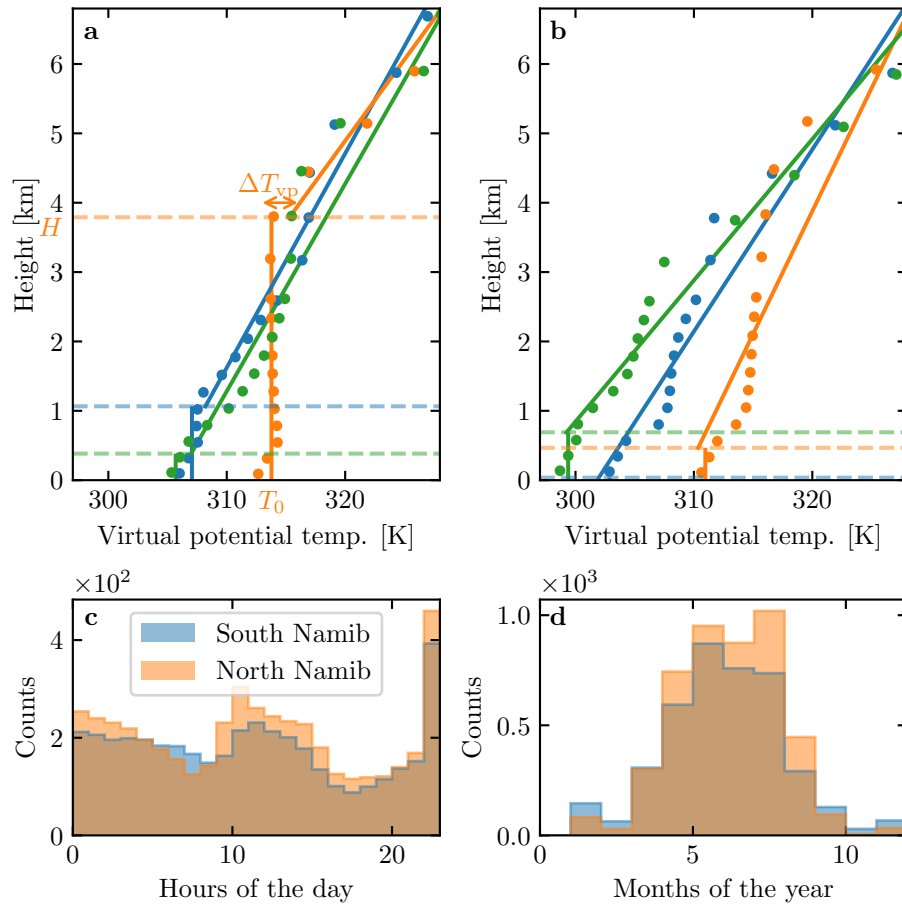


Fig. S10 **a:** Vertical profiles of the virtual potential temperature at three different times (blue: 29/11/2012 - 1100 UTC, orange: 21/03/2017 - 1200 UTC, green: 21/03/2017 - 2000 UTC) at the South Namib station. Dots: data from the ERA5 reanalysis. Dashed lines: boundary layer height given by the ERA5 reanalysis. Plain lines: vertical (ABL) and linear (FA) fits to estimate the quantities displayed in Suppl. Fig. S10. **b:** Examples of ill-processed vertical profiles at three different times (blue: 2/12/2013 - 2300 UTC, orange: 20/03/2017 - 0000 UTC, green: 14/07/2017 - 1400 UTC) at the South Namib station. **c:** Hourly distribution of ill-processed vertical profiles. **d:** Monthly distribution of ill-processed vertical profiles.

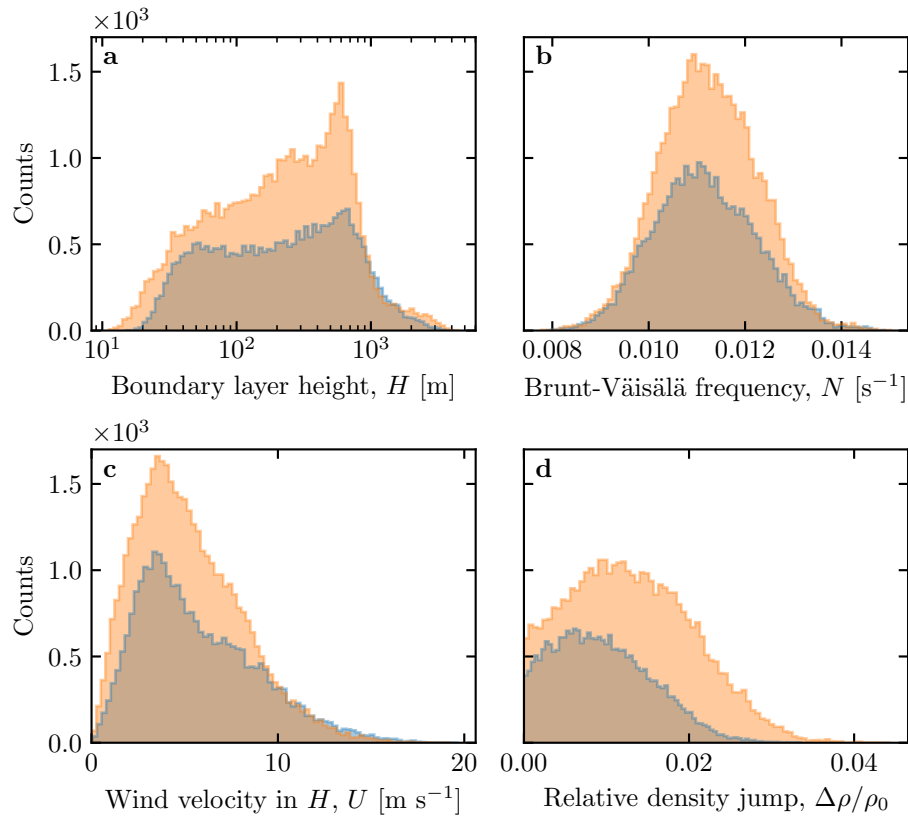


Fig. S11 Distributions of the meteorological parameters resulting from the processing of the ERA5-Land data for the South Namib (blue) and the North Namib (orange) stations.
axis label : panel c -velocity at (height) H. Is this for all day/night/seasons ?

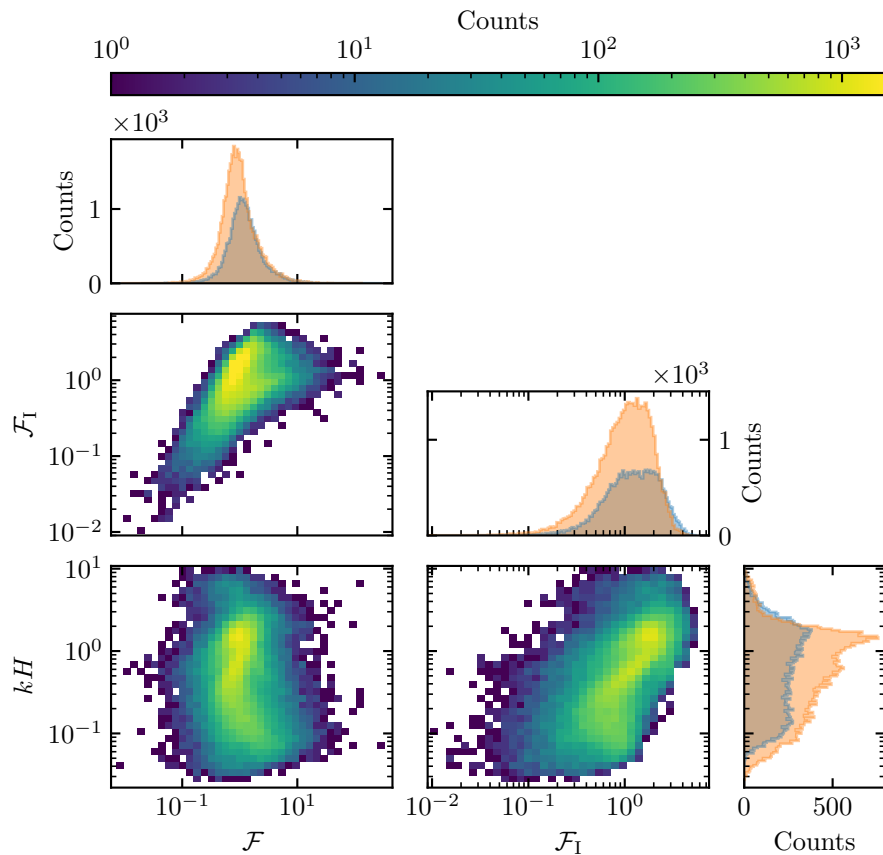


Fig. S12 Non-dimensional parameters distributions. For the marginal ?? distributions, the orange correspond to the South Namib station, and the blue to the North Namib station.

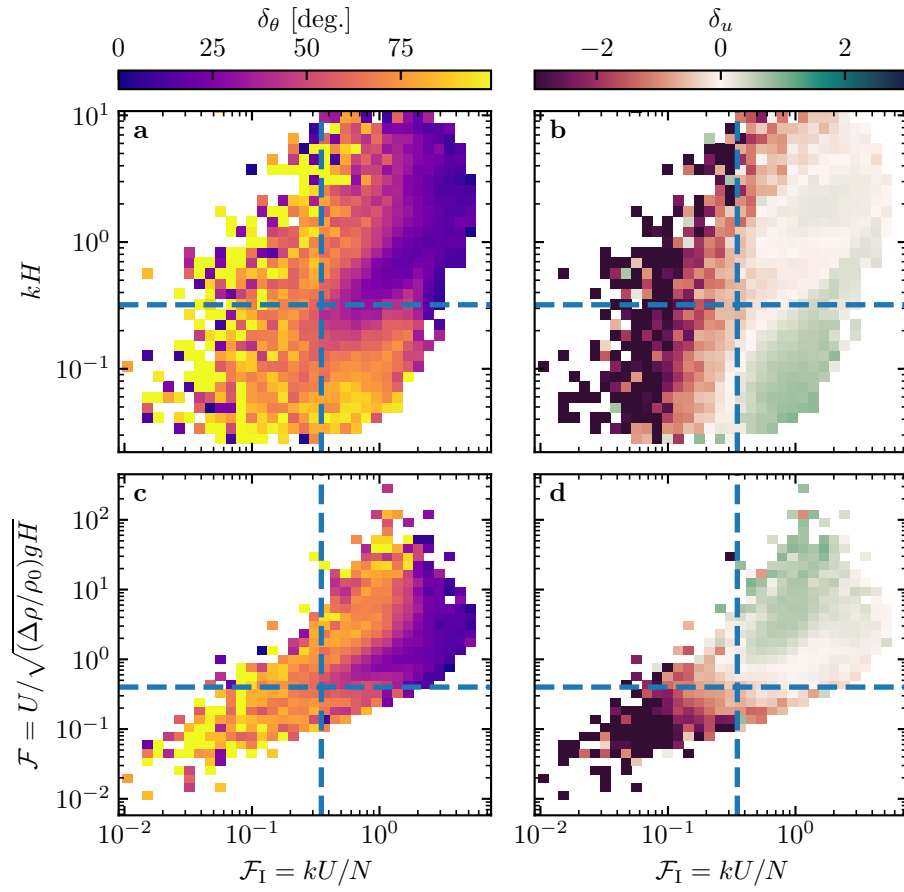


Fig. S13 Regime diagrams of the wind deviation δ_θ and relative attenuation/amplification δ_u in the spaces (\mathcal{F}_I, kH) and $(\mathcal{F}_I, \mathcal{F})$, containing the data from both the North Namib and South Namib stations. Blue dashed lines empirically delimit the different regimes. The point density in each bin of the diagrams is shown in Suppl. Fig. S11. The similar regime diagrams in the space (\mathcal{F}, kH) are shown in Fig. 5.

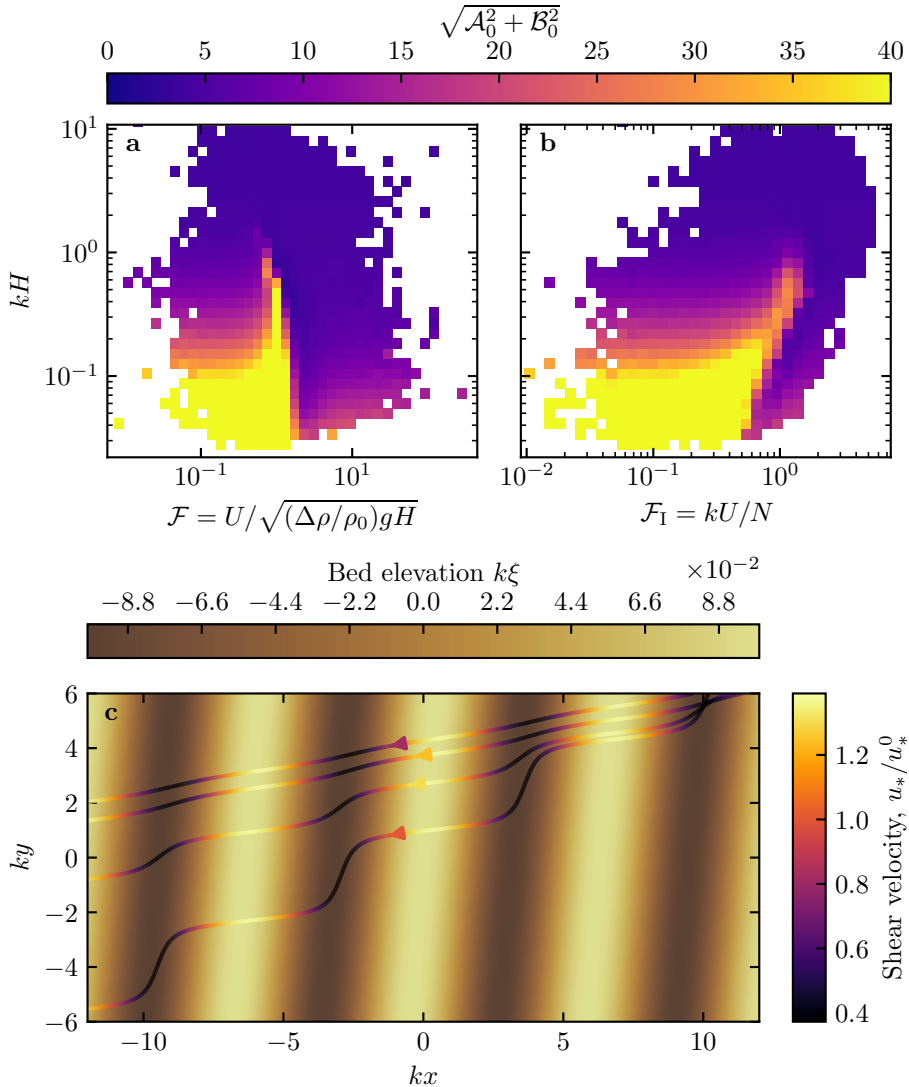


Fig. S14 Computation of the flow disturbance with the linear model of Andreotti et al. (2009). (a) and (b) Magnitude of the hydrodynamic coefficients A_0 and B_0 , calculated from the values of the non-dimensional numbers corresponding to the ERA5-Land time series presented in Figs. 4 and 5. (c) Shear velocity streamlines over sinusoidal ridges of amplitude $k\xi_0 = 0.1$ and for increasing values of $\sqrt{A_0^2 + B_0^2}$. From the upper to the lower streamline, values of $(kH, \mathcal{F}, \mathcal{F}_I, A_0, B_0, \sqrt{A_0^2 + B_0^2})$ are $(1.9, 0.6, 1.5, 3.4, 1.0, 3.5)$, $(1.5, 0.3, 0.4, 4.8, 1.4, 5.0)$, $(0.1, 3.5, 1.0, 8.6, 0.1, 8.6)$, $(0.5, 0.05, 0.04, 9.6, 2.5, 9.9)$.